 ORIGINAL PAGE IS
OF POOR QUALITY

LEWIS GRANT
IN-29-CR
199003
650.

**COMPUTER SIMULATION OF
MACROSEGREGATION IN DIRECTIONALLY
SOLIDIFIED CIRCULAR INGOTS**

by

K. S. Yeum and D. R. Poirier

Department of Materials Science and Engineering

The University of Arizona

Tucson, Arizona 85721

**Prepared as a part of Research Grant NAG 3 723,
"The Role of Gravity on Macrosegregation in Alloys",
The National Aeronautics and Space Administration**

January 7, 1988

**(NASA-CR-182838) COMPUTER SIMULATION OF
MACROSEGREGATION IN DIRECTIONALLY SOLIDIFIED
CIRCULAR INGOTS (Arizona Univ.) 65 p**

CSCI 22A

N89-21134

G3/29

**Unclas
C199003**

ABSTRACT

This is a program report which describes the formulation and employment of a computer code designed to simulate the directional solidification of lead-rich Pb-Sn alloys in the form of an ingot with a uniform and circular cross-section. In this program report, the formulation is for steady-state solidification in which convection in the all-liquid zone is ignored. Particular attention has been given to designing a code to simulate the effect of a subtle variation of temperature in the radial direction. This is important because a very small temperature difference between the center and the surface of the ingot (e.g., less than 0.5 °C) is enough to cause substantial convection within the mushy-zone when the solidification rate is approximately 10^{-3} to 10^{-4} cm · s⁻¹.

TABLE OF CONTENTS

LIST OF SYMBOLS	v
1 INTRODUCTION	1
2 PROBLEM STATEMENT	1
3 CONSERVATION AND FLOW EQUATIONS	2
3.1 Mass Conservation	4
3.2 Local Solute Redistribution	4
3.3 Pressure Equation	7
3.4 Steady-state Solidification	8
3.5 Boundary Conditions	9
3.6 Energy Equation	11
3.7 Macrosegregation	13
4 NUMERICAL METHODS	13
4.1 Nonorthogonal Mesh	15
4.2 Generalized Finite Difference Method	17
4.3 Iterative Computation	22
4.4 Evaluation of Coefficients in Pressure Equation	23
4.5 Solution of Pressure Equation	23
4.6 Computation of Velocities	26
4.7 Quadratic Interpolation	27
4.8 Estimation of Volume Fraction Liquid	27
4.9 Temperature Calculation	28

4.10	Macrosegregation Calculation	29
4.11	Termination of iterations	29
5	EMPLOYING THE CODE	30
5.1	Program Options (Menus)	31
5.2	Output	33
	REFERENCES	34
	APPENDIX - DATA FOR PB-SN ALLOY	54
A.1	Density of Solid	54
A.2	Density of Liquid	54
A.3	Viscosity	54
A.4	Phase Diagram	54
A.5	Primary Dendrite Arm Spacing	55
A.6	Permeability of Interdendritic Liquid	55
A.7	Thermal Conductivity	56
A.8	Enthalpy	56

~~PRECEDING PAGE BLANK NOT FILMED~~

LIST OF SYMBOLS

Subscript

r : r-direction.

z : z-direction.

L : interdendritic liquid.

s : solid

E : eutectic.

i, j : mesh point (i, j) .

o : reference.

$1, 2$: indices for metal components 1 and 2 in a binary alloy, respectively.

$1, 2, \dots, 9$: indices for nine nodes.

SuperScript

(n) : iteration counter.

\bullet : solid/liquid interface.

Others

$-$: average.

$\vec{}$: vector.

Symbols

a, b : geometry of solid/liquid zone (dimensionless).

a_l, s_l, t_l, C_i : constants in equations.

C_L, C_S, C_E, C_S^* : compositions in weight percent Sn of the interdendritic liquid, final solid, eutectic, and the solid at the solid/liquid interface, respectively.

C_{L1}, C_{L2} : concentrations of components 1 and 2 in the interdendritic liquid, respectively (wt. pct.).

$\overline{C_S}$: average composition of the partially solidified solid.

C_{S1}, C_{S2} : concentrations of components 1 and 2 in the solid phase, respectively (wt. pct.).

$\overline{C_\rho}$: average solute concentration per unit volume defined by $\overline{C_\rho} = \overline{C_S} \rho_S + C_L \rho_L$.

$e^{(n)}$: residual in the (n)th iteration step.

f : a function.

\overrightarrow{g} : gravity vector.

g_L, g_S, g_E : volume fractions of the liquid, solid and eutectic, respectively.

g_r, g_z : gravity components in the r- and z-directions, respectively ($\text{cm} \cdot \text{s}^{-2}$).

$H_l, \overline{H_s}$: enthalpy densities of the interdendritic liquid and solid, respectively (*Joule* · g^{-1}).

h_1, h_2, \dots, h_9 : distance to a node from a reference node in the r-direction on the global r-z plane.

K : permeability (cm^2).

k_1, k_2, \dots, k_9 : distance to a node from a reference node in the z-direction on the global r-z plane.

L : entalpy difference defined by $H_l - \overline{H_s}$.

P : pressure ($\text{dyne} \cdot \text{cm}^{-2}$).

P_o : pressure at the reference point, i.e. the intersection of the liquidus isotherm and the centerline of the cylindrical ingot.

\hat{P} : modified pressure defined by $\hat{P} \equiv P - P_o - \rho_{Lo} g_z (z - z_{Lo})$.

Q_l, Q_s : enthalpies of the interdendritic liquid and solid, respectively ($\text{Joule} \cdot \text{g}^{-1}$).

R : radius of the cylindrical ingot (cm).

r, z : distances in the r- and z-directions in a moving coordinate system, respectively.

(r_i, z_i) : coordinate of node i in the r-z global plane.

$(r_{i,j}, z_{i,j})$: coordinate of mesh point (i,j).

r', z' : r and z in the stationary coordinate system, respectively.

T : temperature ($^{\circ}\text{C}$).

t : time (s).

\vec{u} : solidification velocity ($\text{cm} \cdot \text{s}^{-1}$).

u_r, u_z : solidification velocity components in the r- z-directions, respectively ($\text{cm} \cdot \text{s}^{-1}$).

\vec{V} : velocity vector of the interdendritic liquid.

V_r, V_z : interdendritic liquid velocity components in the r- and z-directions, respectively ($\text{cm} \cdot \text{s}^{-1}$).

\vec{w} : velocity of the moving coordinate system ($\text{cm} \cdot \text{s}^{-1}$).

w_r, w_z : velocity components of the moving coordinate system ($\text{cm} \cdot \text{s}^{-1}$).

z_L, z_E : z coordinates of the liquidus and eutectic isotherms, respectively.

z_{Lo} : z coordinate of the reference point, i.e. the intersection of the liquidus isotherm and the centerline of the cylindrical ingot.

$\alpha_1, \alpha_2, \dots, \alpha_9$: distance to a node from a reference node in the r-direction on the local $\alpha - \beta$ plane.

$\alpha_r, \beta_r, \alpha_z, \beta_z$: grouped variables.

$\beta_1, \beta_2, \dots, \beta_9$: distance to a node from a reference node in the z-direction on the local $\alpha - \beta$

plane.

κ : thermal conductivity ($\text{watt} \cdot \text{cm}^{-1} \cdot ^\circ\text{C}^{-1}$).

κ_{L1}, κ_{L2} : thermal conductivities of the pure liquid metals 1 and 2, respectively ($\text{watt} \cdot \text{cm}^{-1} \cdot ^\circ\text{C}^{-1}$).

κ_{S1}, κ_{S2} : thermal conductivities of the pure solid metals 1 and 2, respectively ($\text{watt} \cdot \text{cm}^{-1} \cdot ^\circ\text{C}^{-1}$).

μ : viscosity of the interdendritic liquid (poise).

$\bar{\rho}$: average density defined by $\bar{\rho} \equiv \rho_S g_S + \rho_L g_L$.

ρ_L, ρ_S : densities of the interdendritic liquid and solid, respectively ($\text{g} \cdot \text{cm}^{-3}$).

ρ_{Lo} : density of the liquid at the liquidus isotherm ($\text{g} \cdot \text{cm}^{-3}$).

ρ_{SE}, ρ_{LE} : densities of the liquid and solid of the eutectic composition, respectively ($\text{g} \cdot \text{cm}^{-3}$).

1 INTRODUCTION

This report describes the numerical formulation of a model for the vertical solidification of a binary alloy in a cylindrical mold. This is a preliminary model in that so-called "steady-state" solidification is tested. In the final version, the code will be able to treat a mushy zone that changes with time. The major goal is the estimation of macrosegregation in the cast structure of small ingots, which solidify slowly (less than $0.01 \text{ cm} \cdot \text{s}^{-1}$). Calculations are performed for the solid/liquid zone formed between the liquid and solid regions. Convection in liquid region is neglected, and the flow of interdendritic liquid in the solid/liquid zone is modelled as flow through a porous medium. This flow is induced by gravity and solidification contractions (or expansions).

The temperature field in the zone affects physical properties and the fraction of interdendritic liquid. In order to solve for temperature, the energy equation takes account of the latent heat of freezing during solidification. The flow of the interdendritic liquid satisfies the constraint of the heat flow for steady-state solidification, and then the resulting macrosegregation in the radial direction of cylindrical ingot is computed by averaging the concentrations of primary and eutectic solids.

For a predefined computation zone a generalized finite difference method is employed to obtain a numerical solution of the equations. Nonplanar boundaries corresponding to the top and bottom of the solid/liquid zone are considered so that the effect of a subtle radial temperature gradient on macrosegregation can be simulated.

2 PROBLEM STATEMENT

Fig. 1 shows an ingot of a binary alloy undergoing vertical solidification. Most of

the heat conduction is in the negative z-direction with a very small radial component. Gravity is in the negative z-direction as shown, with no component in the radial direction. It is assumed that dendritic freezing takes place within the mushy zone, which moves upward with a constant velocity. The shape of the eutectic and liquidus isotherms can be flat, convex or concave. The concentrations of solute in the liquid and solid, C_L and C_S , vary in the zone. The convection of the interdendritic liquid driven by shrinkage and gravity, causes nonuniformities in the final average composition, C_S ; this is known as macrosegregation. The effects of shrinkage were first studied by Flemings and Nereo [1], and later both shrinkage and gravity were considered by several, including Maples and Poirier [2], in the analysis of macrosegregation.

The mold shown in Fig. 1 is symmetric about the centerline, and in a steady-state solidification, the geometry of the mushy zone, the temperature distribution, and the velocity field, are all constant in time. Because steady-state solidification is considered, macrosegregation is absent in the z-direction, and macrosegregation in terms of the composition, C_S , is only a function of radius across the ingot. Necessary data for computation are: 1) liquid density as a function of temperature; 2) solid density; 3) the phase diagram for the binary alloy; 4) the permeability for flow of interdendritic liquid; 5) velocity of the solid/liquid zone; and 6) the geometry of the zone. Temperatures and velocity fields are calculated and then macrosegregation is obtained from these results.

3 CONSERVATION AND FLOW EQUATIONS

The flow of interdendritic liquid through the mushy zone is governed by the principles of conservation of mass, solute, momentum and energy. The solution to the conservation

equations requires extensive computations; however, these equations can be simplified without losing accuracy for the macrosegregation problem of our interest. Fig. 2 illustrates the derivation of the simplified equations. The equation for the momentum conservation is replaced by D'Arcy's Law, which describes the flow of the interdendritic liquid through a porous medium. Hubbert[3] proved that D'Arcy's is valid when the flow velocity is low such that inertial forces are negligible compared with those arising from viscosity. A combination of this equation with mass conservation results in the pressure equation. Other combinations of the energy and solute conservations with the mass conservation lead to a simplified energy equation and the solute redistribution equation, respectively.

This formulation is effective in reducing the computational effort required for calculation of macrosegregation. The variables to be computed are pressure (P), velocities in the r - and z -directions (V_r , V_z), volume fraction liquid (g_L), and the temperature (T). Starting from a initial guess of these values, the variables are updated as indicated in Fig. 2. The curved arrows pointing to the equations indicate the order of the updating process. When the computed pressure is sufficiently accurate, the iteration is terminated. The derivation of the equations enclosed by circles in Fig. 2 are described in this section.

Following Flemings and Nereo [1], the assumptions used in deriving the equations are summarized below:

- a) no movement of solid,
- b) no flux by diffusion in the liquid in the direction of the thermal gradient,
- c) constant solid density,
- d) no pore formation, and

e) no diffusion of solute in solid.

3.1 Mass Conservation.

By taking account of the convection of liquid, the mass conservation is

$$\frac{\partial \bar{p}}{\partial t} = -\nabla \cdot (\rho_L g_L \vec{V}) \quad (3.1.1)$$

where

$$\bar{p} = \rho_S g_S + \rho_L g_L . \quad (3.1.2)$$

If porosity is not formed, we have

$$g_S + g_L = 1 \quad (3.1.3)$$

and

$$\frac{\partial g_S}{\partial t} + \frac{\partial g_L}{\partial t} = 0 . \quad (3.1.4)$$

By inserting Eqs. (3.1.2) through (3.1.4) into Eq. (3.1.1), we obtain

$$-\nabla \cdot (\rho_L g_L \vec{V}) = (\rho_L - \rho_S) \frac{\partial g_L}{\partial t} + g_L \frac{\partial \rho_L}{\partial t} . \quad (3.1.5)$$

3.2 Local Solute Redistribution.

The local solute redistribution was first derived by Flemings and Nereo [1]. Some steps omitted in the derivation are resolved in the derivation shown below.

Similar to Eq. (3.1.1) conservation of solute is

$$\frac{\partial \overline{C\rho}}{\partial t} = -\nabla \cdot (C_L \rho_L g_L \vec{V}) \quad (3.2.1)$$

where

$$\overline{C\rho} = \overline{C}_S \rho_S g_S + C_L \rho_L g_L . \quad (3.2.2)$$

Expanding the right hand side of Eq. (3.2.1) we have

$$\frac{\partial \overline{C\rho}}{\partial t} = -C_L \nabla \cdot (\rho_L g_L \vec{V}) - \rho_L g_L \vec{V} \cdot \nabla C_L \quad (3.2.3)$$

and substitution of Eq. (3.1.1) gives

$$-\rho_L g_L \vec{V} \cdot \nabla C_L = \frac{\partial \overline{C\rho}}{\partial t} - C_L \frac{\partial \overline{p}}{\partial t} . \quad (3.2.4)$$

The first derivative term on the right hand side of Eq. (3.2.4) is rewritten

$$\frac{\partial \overline{C\rho}}{\partial t} = \rho_S \frac{\partial \overline{C_S g_S}}{\partial t} + C_L \frac{\partial \rho_L g_L}{\partial t} + \rho_L g_L \frac{\partial C_L}{\partial t} \quad (3.2.5)$$

by substituting Eq. (3.2.2) for $\overline{C\rho}$ and expanding into several terms. By replacing the $\rho_L g_L$ in the second term of the right hand side of this equation with $(\overline{p} - \rho_S g_S)$ and rearranging, we obtain

$$\frac{\partial \overline{C\rho}}{\partial t} = \rho_S \frac{\partial \overline{C_S g_S}}{\partial t} - C_L \frac{\partial \rho_S g_S}{\partial t} + \rho_L g_L \frac{\partial C_L}{\partial t} . \quad (3.2.6)$$

Substitution of this expression into the first derivative term on the right hand side of Eq. (3.2.4) gives

$$-\rho_L g_L \vec{V} \cdot \nabla C_L = \rho_S \frac{\partial \overline{C_S g_S}}{\partial t} + C_L \frac{\partial \overline{p}}{\partial t} - C_L \frac{\partial \rho_S g_S}{\partial t} + \rho_L g_L \frac{\partial C_L}{\partial t} . \quad (3.2.7)$$

Let's consider rewriting the first term in this equation. The average solid composition, $\overline{C_S}$, is

$$\overline{C_S} = \frac{1}{g_S} \int_0^{g_S} C_S^* dg_S , \quad (3.2.8)$$

where C_S^* is the solid concentration at the solid-liquid interface. According to Leibnitz's rule,

$$\frac{d(\overline{C_S g_S})}{dt} = \int_0^{g_S} \frac{\partial C_S^*}{\partial t} dg_S + C_S^* \frac{dg_S}{dt} , \quad (3.2.9)$$

and according to Fick's second law of diffusion, the change in C_S^* at a fixed location is expressed with

$$\frac{\partial C_S^*}{\partial t} = D_S \frac{\partial^2 C_S^*}{\partial z^2} \quad (3.2.10)$$

where D_S is the diffusion coefficient of the solute in the solid. If the diffusion of the solute in solid is neglected ($D_S = 0$), Eq. (3.2.9) becomes

$$\frac{d\overline{C_S} g_S}{dt} = C_S^* \frac{\partial g_S}{\partial t} . \quad (3.2.11)$$

Note that $\overline{C_S}$ and g_S are functions of time and space. With respect to a stationary coordinate, following relations are valid:

$$\frac{d\overline{C_S} g_S}{dt} = \frac{\partial \overline{C_S} g_S}{\partial t} , \quad (3.2.12)$$

and

$$\frac{dg_S}{dt} = \frac{\partial g_S}{\partial t} . \quad (3.2.13)$$

Thus Eq. (3.2.11) is reduced to

$$\frac{\partial \overline{C_S} g_S}{\partial t} = C_S^* \frac{\partial g_S}{\partial t} . \quad (3.2.14)$$

Flemings and Nereo [1] presented this equation without showing the steps given above. By substituting Eqs. (3.2.9) and (3.2.14) into Eq. (3.2.13), we obtain

$$\frac{1}{g_L} \frac{\partial g_L}{\partial t} = - \frac{\rho_L}{\rho_S} \frac{1}{C_L} \frac{1}{(1-k)} \vec{V} \cdot \nabla C_L + \frac{\partial C_L}{\partial t} \quad (3.2.15)$$

where k is the equilibrium partition ratio, defined by $k = C_S^*/C_L$. Equation (3.2.15) is known as the "solute redistribution equation", and it relates the dependency of the volume fraction liquid on the solute concentration and the velocity of the interdendritic liquid. The values of ρ_L , ρ_S and k are functions of temperature and hence of C_L .

3.3 Pressure Equation.

The flow of the interdendritic liquid is expressed with D'Arcy's Law; hence

$$\vec{V} = -\frac{K}{\mu g_L}(\nabla P - \rho_L \vec{g}) \quad (3.3.1)$$

where μ is the viscosity of the liquid and K is the permeability of the dendritic network. If the pressure is considered with reference to atmospheric pressure and the density of liquid at the liquidus isotherm, we define \hat{P} with

$$\hat{P} = P - P_o - \rho_{Lo} g_z (z - z_{Lo}) - \rho_{Lo} g_r r \quad (3.3.2)$$

then Eq. (3.3.1) can be rewritten

$$\vec{V} = -\frac{K}{\mu g_L} \left[\nabla \hat{P} - (\rho_L - \rho_{Lo}) \vec{g} \right] \quad (3.3.3)$$

The two velocity components, V_r and V_z , in cylindrical coordinate system are given by:

$$V_r = -\frac{K_r}{\mu g_L} \left[\frac{\partial \hat{P}}{\partial r} - (\rho_L - \rho_{Lo}) g_r \right] \quad (3.3.4)$$

and

$$V_z = -\frac{K_z}{\mu g_L} \left[\frac{\partial \hat{P}}{\partial z} - (\rho_L - \rho_{Lo}) g_z \right] \quad (3.3.5)$$

where K_r and K_z are the permeabilities in the r - and z -directions, respectively, and g_r and g_z are zero and $-g$, respectively, for vertical solidification.

In cylindrical coordinates the left hand side of Eq. (3.1.5) is

$$-\nabla \cdot (\rho_L g_L \vec{V}) = -\frac{1}{r} \frac{\partial (\rho_L g_L V_r)}{\partial r} - \frac{\partial (\rho_L g_L V_z)}{\partial z} \quad (3.3.6)$$

and substitution of Eqs. (3.3.4) and (3.3.5) into Eq. (3.3.6) leads to the pressure equation, which is

$$\begin{aligned} \alpha_r \frac{\partial^2 \hat{P}}{\partial r^2} + \left(\frac{\alpha_r}{r} + \frac{\partial \alpha_r}{\partial r} \right) \frac{\partial \hat{P}}{\partial r} + \alpha_z \frac{\partial^2 \hat{P}}{\partial z^2} + \frac{\partial \alpha_z}{\partial z} \frac{\partial \hat{P}}{\partial z} \\ = (\rho_L - \rho_S) \frac{\partial g_L}{\partial t} + g_L \frac{\partial \rho_L}{\partial t} + \left(\frac{\partial \beta_z}{\partial z} - \rho_{Lo} \frac{\partial \alpha_z}{\partial z} \right) g_z \end{aligned} \quad (3.3.7)$$

where

$$\alpha_r \equiv \frac{K_r \rho_L}{\mu} ,$$

$$\beta_r \equiv \rho_L \alpha_r ,$$

$$\alpha_z \equiv \frac{K_z \rho_L}{\mu} ,$$

$$\beta_z \equiv \rho_L \alpha_z .$$

It should be pointed out that K_r and K_z each vary within the solid/liquid zone according to the volume fraction of liquid and the dendrite arm spacings of the dendritic network [4].

3.4 Steady-state Solidification.

Consider a stationary coordinate (r', z') and a moving coordinate system (r, z) with the velocity (w_r, w_z) . Then a full derivative of a function f with respect to t is given by

$$\frac{\partial f(r', z', t)}{\partial t} = \frac{\partial f(r, z, t)}{\partial t} - w_r \frac{\partial f(r, z, t)}{\partial r} - w_z \frac{\partial f(r, z, t)}{\partial z} . \quad (3.4.1)$$

For steady-state, the function value on a moving frame does not change with time. Thus we have

$$\frac{\partial f(r', z', t)}{\partial t} = -\vec{w} \cdot \nabla f(r, z) . \quad (3.4.2)$$

For our application the origin moves such that $w_r = 0$ and $w_z = u_z$, where u_z is the solidification velocity in the z-direction, then Eqs. (3.2.15) and (3.3.7) are reduced to the following expressions:

$$\begin{aligned} \alpha_r \frac{\partial^2 \hat{P}}{\partial r^2} + \left(\frac{\alpha_r}{r} + \frac{\partial \alpha_r}{\partial r} \right) \frac{\partial \hat{P}}{\partial r} + \alpha_z \frac{\partial^2 \hat{P}}{\partial z^2} + \frac{\partial \alpha_z}{\partial z} \frac{\partial \hat{P}}{\partial z} \\ = -u_z \left[(\rho_L - \rho_S) \frac{\partial g_L}{\partial z} + g_L \frac{\partial \rho_L}{\partial z} \right] \\ + \left(\frac{\partial \beta_z}{\partial z} - \rho_{Lo} \frac{\partial \alpha_z}{\partial z} \right) g_z \end{aligned} \quad (3.4.2)$$

and

$$u_z \frac{\partial \ln g_L}{\partial z} = \frac{\rho_L}{\rho_S} \frac{1}{(1-k)} \left[V_r \frac{\partial \ln C_L}{\partial r} + (V_z - u_z) \frac{\partial \ln C_L}{\partial z} \right] \quad (3.4.3)$$

Equations (3.4.2) and (3.4.3) are the pressure equation and solute redistribution equation, respectively, for steady-state solidification.

At $r = 0$, we evaluate $(\alpha_r/r) (\partial \hat{P}/\partial r)$ with L'Hospital's rule; therefore

$$\lim_{r \rightarrow 0} \left(\frac{\alpha_r}{r} \frac{\partial \hat{P}}{\partial r} \right) = \frac{\partial \alpha_r}{\partial r} \frac{\partial \hat{P}}{\partial r} + \alpha_r \frac{\partial^2 \hat{P}}{\partial r^2} \quad (3.4.4)$$

3.5 Boundary Conditions.

At the liquidus isotherm

If the pressure at $r = 0$ and at the isotherm is represented with P_o , then the pressure along the liquidus isotherm is

$$P = P_o + \rho_{Lo} g_z (z - z_{Lo}) \quad (3.5.1)$$

where g_z is the component of gravity in the z-direction and ρ_{Lo} is the density of the interdendritic liquid where $C_L = C_o$. In terms of the modified pressure \hat{P} , related to by Eq. (3.3.2), this condition becomes

$$\hat{P} = 0. \quad (3.5.2)$$

At the eutectic isotherm

Interdendritic liquid must flow to compensate for the shrinkage associated with the solidification of the eutectic liquid. Thus,

$$V_r = -u_z \left(\frac{\rho_{SE} - \rho_{LE}}{\rho_{LE}} \right) (-\tan \theta), \quad (3.5.3)$$

and

$$V_z = -u_z \left(\frac{\rho_{SE} - \rho_{LE}}{\rho_{LE}} \right) \quad (3.5.4)$$

where θ is the angle between the tangent to the eutectic isotherm and the horizontal line. By combining Eqs. (3.3.5, (3.5.3) and (3.5.4), the boundary condition can be expressed in terms of the pressure gradient at the eutectic isotherm

$$\frac{\partial \hat{P}}{\partial r} = \frac{\mu g_L}{K_r} u_z \left(\frac{\rho_{SE}}{\rho_{LE}} - 1 \right) (-\tan \theta) + (\rho_L - \rho_{Lo}) g_r \quad (3.5.5)$$

$$\frac{\partial \hat{P}}{\partial z} = \frac{\mu g_L}{K_z} u_z \left(\frac{\rho_{SE}}{\rho_{LE}} - 1 \right) + (\rho_L - \rho_{Lo}) g_z \quad (3.5.6)$$

At the center ($r=0$)

Since the solid/liquid zone is axisymmetric, the radial component of velocity is zero.

$$V_r = 0.$$

Substitution of this equation into Eq. (3.3.4) gives

$$\frac{\partial \hat{P}}{\partial r} = 0. \quad (3.5.7)$$

At the outer wall ($r=R$)

The outer wall blocks the movement of the interdendritic liquid in the r -direction.

Thus

$$V_r = 0$$

so in terms of modified pressure,

$$\frac{\partial \hat{P}}{\partial r} = 0. \quad (3.5.8)$$

The boundary conditions are also shown in Figs 3(a) and 3(b). Temperatures at the eutectic and liquidus isotherms are T_E and T_o , respectively, and the axial symmetry gives zero heat flux in the radial direction at the center, i.e. $\partial T / \partial r = 0$.

3.6 Energy Equation.

Let's represent the enthalpy densities for the solid and the interdendritic liquid with Q_s and Q_l , respectively. The energy conservation, taking account of heat conduction and convection, is

$$\frac{\partial}{\partial t}(Q_s + Q_l) = \nabla \cdot (\kappa \nabla T) - \nabla(Q_l \vec{V}) \quad (3.6.1)$$

where κ is the thermal conductivity of the mixture of the solid and liquid. The first term on the r.h.s. of Eq. (3.6.1) is the energy transported due to conduction and the second due to the convection of the interdendritic liquid. The enthalpy densities are related to the enthalpy of the primary solid, H_s , and the enthalpy of the interdendritic liquid, H_l , through the equations,

$$Q_s = \rho_s g_s H_s \quad (3.6.2)$$

and

$$Q_l = \rho_L g_L H_l \quad (3.6.3)$$

If we define the difference in the enthalpies, L , with

$$L \equiv H_l - H_s \quad (3.6.4)$$

then Eq. (3.6.3) becomes

$$Q_t = \rho_L g_L \bar{H}_s + \rho_L g_L L. \quad (3.6.5)$$

Substituting Eqs. (3.6.2) and (3.6.5) into Eq. (3.6.1) and expanding terms, we obtain

$$\begin{aligned} \bar{H}_s \frac{\partial \bar{p}}{\partial t} + \bar{p} \frac{\partial \bar{H}_s}{\partial t} + \rho_L g_L \frac{\partial L}{\partial t} + L \frac{\partial \rho_L g_L}{\partial t} \\ = \nabla \cdot (\kappa \nabla T) - \bar{H}_s \nabla (\rho_L g_L \bar{V}) - \rho_L g_L \bar{V} \cdot \nabla \bar{H}_s \\ - L \nabla (\rho_L g_L \bar{V}) - \rho_L g_L \bar{V} \cdot \nabla L \end{aligned} \quad (3.6.6)$$

where \bar{p} is the average density given by Eq. (3.1.2), and inserting Eqs. (3.1.1) and (3.1.2) into Eq. (3.6.6) to eliminate $\nabla \cdot (\rho_L g_L \bar{V})$ terms, we obtain

$$\bar{p} \frac{\partial \bar{H}_s}{\partial t} + \rho_L g_L \frac{\partial L}{\partial t} - L \frac{\partial \rho_S g_S}{\partial t} = -\rho_L g_L \bar{V} \cdot (\nabla \bar{H}_s + \nabla L). \quad (3.6.7)$$

For steady-state solidification and a moving coordinate system with velocity components $w_r = 0$ and $w_z = u_z$, we can write

$$\kappa_r \frac{\partial^2 T}{\partial r^2} + \kappa_z \frac{\partial^2 T}{\partial z^2} + \left(\frac{\kappa_r}{r} + \frac{\partial \kappa_r}{\partial r} \right) \frac{\partial T}{\partial r} + \frac{\partial \kappa_z}{\partial z} \frac{\partial T}{\partial z} = C \quad (3.6.8)$$

where

$$\begin{aligned} C = -L \rho_S u_z \frac{\partial g_L}{\partial z} + \rho_L g_L \left[V_r \frac{\partial L}{\partial r} + (V_z - u_z) \frac{\partial L}{\partial z} \right] \\ + \rho_L g_L V_r \frac{\partial \bar{H}_s}{\partial r} + (\rho_L g_L V_z - \bar{p} u_z) \frac{\partial \bar{H}_s}{\partial z}. \end{aligned}$$

Equation (3.6.8) is obtained by replacing the time derivative terms in Eq. (3.6.7) with space derivatives via Eq. (3.4.2) and by using the assumptions of a constant solid density and no porosity formation. The thermal conductivities in the r- and z-directions, κ_r and κ_z , are approximated with the following formulas:

$$\kappa_r \approx \frac{1}{(1 - g_L)/\kappa_s + g_L/\kappa_L} \quad (3.6.9)$$

$$\kappa_z \approx (1 - g_L)\kappa_s + g_L\kappa_L \quad (3.6.10)$$

where the thermal conductivities of the solid and the interdendritic liquid, κ_s and κ_L , are obtained from the thermal data for the pure solids and liquids of the components of the binary alloy:

$$\kappa_s \approx \frac{C_{s1}\kappa_{s1} + C_{s2}\kappa_{s2}}{100} \quad (3.6.11)$$

and

$$\kappa_L \approx \frac{C_{L1}\kappa_{L1} + C_{L2}\kappa_{L2}}{100} \quad (3.6.12)$$

3.7. Macrosegregation. The local average composition in a casting after complete solidification is obtained by averaging the compositions of the primary and eutectic solids.

Therefore

$$C_S = \frac{\rho_S(1 - g_E)\overline{C_S} + \rho_{SE}g_EC_E}{\rho_S(1 - g_E) + \rho_{SE}g_E} \quad (3.7.1)$$

The volume fraction of solid at the eutectic isotherm is $(1 - g_E)$ and replacing $\overline{C_S}$ with Eq. (3.2.8) gives

$$C_S = \frac{\int_0^{1-g_E} \rho_S C_S^* dg_S + \rho_{SE}g_EC_E}{\rho_S(1 - g_E) + \rho_{SE}g_E} \quad (3.7.2)$$

For steady-state solidification C_S is dependent on radius. Integration is performed from the liquidus to the eutectic isotherms in the z -direction at a constant radius.

4 NUMERICAL METHODS

In directional solidification processes, it is advantageous to effect vertical solidification with perfectly horizontal isotherms. With such a thermal field no macrosegregation across the ingot or casting results, and there is also little or no macrosegregation along the direction of solidification. However, to maintain perfectly horizontal isotherms implies

no temperature gradients across the ingot or casting; this, of course, is impossible but is approximated in practice.

The consequence of slightly curved isotherms is that there can be macrosegregation across the casting or ingot depending upon solidification rate, the alloy, and the extent of the concavity or convexity of the isotherms. At high solidification rates, e.g. $u_z > 5 \times 10^{-2} \text{ cm} \cdot \text{s}^{-1}$, a small curvature of the isotherms is expected to be insignificant, but at low solidification rates, e.g. $10^{-2} \leq u_z \leq 10^{-4} \text{ cm} \cdot \text{s}^{-1}$, even slight curvatures can profoundly affect the flow of the interdendritic liquid and, thereby, cause macrosegregation.

In the following we discuss first the numerical simulation of a rectangular mesh, which is approximate for directional solidification (DS) with horizontal isotherms, and then we discuss a non-rectangular mesh for adaptation to DS slightly curved isotherms.

The generation of a rectangular mesh is straightforward; however there are some difficulties in formulating finite difference approximations for boundary points. Fig. 4(a) shows a rectangular mesh with uniform spacings in the r - and z -directions as employed by Kou [5]. At the curved boundaries there are special cases which require carefully written finite difference approximations of the derivatives. Usually finite difference equations of the second order accuracy are mostly considered, and the truncation errors involved in the approximations are proportional to the square of the grid spacings. In order to retain accuracy, all points including the boundary points must be expressed with the formulas of at least the same order of the accuracy of the interior points. For irregular boundary points, complicated expressions are required and various formulas must be considered for different cases. As an example, the first derivative of the function normal to the boundary

for point A shown in Fig. 4(a) can be expressed with values at its five nearest points and the point itself to get the second order accuracy of the derivative. The expression must be dependent on the distances from boundary points to a internal point closest to point A in the r - and z -directions. It can be seen that point B must be considered in terms of the six points shown as circles in Fig. 4(a). This kind of treatment necessitates complex book-keeping.

To overcome the problems of the mesh of Fig. 4(a), Ridder et al.[6] employed a grid design shown in Fig. 4(b). Vertical lines of equal spacings in the r -direction are drawn and the horizontal lines are drawn beginning at the intersections of curved boundaries and the vertical lines, resulting in nonuniform grid spacings in the z -direction. Additional horizontal lines which do not cross the curved boundaries are also inserted if necessary. This configuration gives computational efficiency and eliminates the burden of complex book-keeping for the mesh points at the curved boundaries; however, it must be noted that spacings in the z -directions are dependent on the selection of vertical grid lines, and the grid spacings of consecutive mesh points may differ by as much as several order of magnitudes depending on the geometry of the computation domain. This can adversely affect the accuracy of the solution as well as the convergence properties of the difference method.

4.1 Nonorthogonal Mesh.

A nonorthogonal mesh is shown in Fig. 5. Suppose that we want m intervals in the r -direction and n intervals in the z -direction; we can start with $(n - 1)$ equally-spaced points at the center line, i.e., $r=0$. Arbitrary smooth cuves are drawn toward the outer wall of the

cylinder from these points. Vertical lines equidistant in the r -direction are drawn. Let's number the mesh points in the computational domain with two indices, i and j ; i equals 1 for the points on the center line and $(m+1)$ for those at $r=R$, and j equals 1 for the points on the eutectic isotherm and $(n+1)$ for those on the liquidus isotherm. The eutectic and liquidus isotherms are written as

$$z_E = a \left[2 \left(\frac{r}{R} \right)^2 - \left(\frac{r}{R} \right)^4 \right] \quad (4.1.1)$$

and

$$z_L = b \left[2 \left(\frac{r}{R} \right)^2 - \left(\frac{r}{R} \right)^4 \right] + c \quad (4.1.2)$$

where R is the radius of the cylinder. The coordinates of the point (i, j) are

$$r_{i,j} = R \frac{(i-1)}{m} \quad (4.1.3)$$

and

$$z_{i,j} = (bp)_j \left[2 \left(\frac{r_{i,j}}{R} \right)^2 - \left(\frac{r_{i,j}}{R} \right)^4 \right] + (cp)_j \quad (4.1.4)$$

where

$$(bp)_j = a \left(1 - \frac{j-1}{n} \right) + b \frac{j-1}{n} \quad (4.1.5)$$

and

$$(cp)_j = c \frac{j-1}{n} \quad (4.1.6)$$

Also the tangent to the curve is given by

$$(\tan \theta)_{i,j} = 4(bp)_j \frac{r_{i,j}}{R^2} \left[1 - \left(\frac{r_{i,j}}{R} \right)^2 \right] \quad (4.1.7)$$

This simple scheme assures that the ratios of the adjacent grid spacings in the r - and z -directions are close to unity and the curves are smooth. This is beneficial to the proper

estimation of spatial derivatives, however, it is necessary to consider finite difference approximations that are different than conventional expressions, because the generated mesh is nonorthogonal. A detailed description of this approximation is given later.

4.2 Generalized Finite Difference Method.

Conventional finite difference methods divide a computation domain into rectangular meshes by positioning mesh points along a curve parallel to either of the orthogonal axes, and approximate spatial derivatives with several function values along the curve. Consider the rectangular meshes of the uniform spacings in the r - and z -directions as shown in Fig. 6(a). Central difference approximations of the first and second derivatives of a function f at a mesh point (i, j) are represented with the following relations:

$$\begin{aligned}\frac{\partial f}{\partial r} &= \frac{f_{i+1,j} - f_{i-1,j}}{2\Delta r} \\ \frac{\partial f}{\partial z} &= \frac{f_{i,j+1} - f_{i,j-1}}{2\Delta z} \\ \frac{\partial^2 f}{\partial r^2} &= \frac{f_{i+1,j} - 2f_{i,j} + f_{i-1,j}}{(\Delta r)^2} \\ \frac{\partial^2 f}{\partial r \partial z} &= \frac{f_{i+1,j-1} + f_{i+1,j+1} - f_{i-1,j+1} + f_{i-1,j-1}}{4\Delta r \Delta z}\end{aligned}$$

and

$$\frac{\partial^2 f}{\partial z^2} = \frac{f_{i,j+1} - 2f_{i,j} + f_{i,j-1}}{(\Delta z)^2}$$

The derivatives are given in terms of the grid spacings and the function values at neighboring eight points and the point itself. In matrix notation these equations may be rewritten,

$$(GD) = (TR)(f_N) \tag{4.2.1}$$

where

$$(GD) = \begin{pmatrix} \partial f / \partial r \\ \partial f / \partial z \\ \partial^2 f / \partial r^2 \\ \partial^2 f / \partial r \partial z \\ \partial^2 f / \partial z^2 \end{pmatrix} \quad (4.2.2)$$

$$(TR) = \begin{pmatrix} 0 & \frac{0.5}{\Delta r} & 0 & -\frac{0.5}{\Delta r} & 0 & 0 & 0 & 0 & 0 \\ 0 & 0 & \frac{0.5}{\Delta z} & 0 & -\frac{0.5}{\Delta z} & 0 & 0 & 0 & 0 \\ -\frac{2.0}{(\Delta r)^2} & \frac{1.0}{(\Delta r)^2} & 0 & \frac{1.0}{(\Delta r)^2} & 0 & 0 & 0 & 0 & 0 \\ -\frac{2.0}{(\Delta z)^2} & 0 & \frac{1.0}{(\Delta z)^2} & 0 & \frac{1.0}{(\Delta z)^2} & 0 & 0 & 0 & 0 \\ 0 & 0 & 0 & 0 & 0 & -\frac{0.25}{\Delta r \Delta z} & \frac{0.25}{\Delta r \Delta z} & -\frac{0.25}{\Delta r \Delta z} & \frac{0.25}{\Delta r \Delta z} \end{pmatrix} \quad (4.2.3)$$

and

$$(f_N) = \begin{pmatrix} f_{i,j} \\ f_{i+1,j} \\ f_{i,j+1} \\ f_{i-1,j} \\ f_{i,j-1} \\ f_{i+1,j-1} \\ f_{i+1,j+1} \\ f_{i+1,j-1} \\ f_{i-1,j-1} \end{pmatrix} \quad (4.2.4)$$

where column vectors (GD) and (f_N) represent the global derivatives and nodal function values, respectively, and the (TR) a 5×9 transformation matrix which makes it possible to compute (GD) based on nodal function values. Examination of Eq. (4.2.1) shows that the shape of the matrix (TR) is dependent on Δr and Δz . Suppose that the grid lines are not parallel to the axes of the coordinates. Then, all the zeros in Eq. (4.2.1) are expected to be changed to nonzeros. This indicates that (GD) is dependent on the location of the neighboring points. Instead of taking the center node as a reference, any of the other eight neighboring nodes can be selected as the reference and employ forward and/or backward differencing techniques in either of the directions.

The dependency of the (TR) on the coordinates of the neighboring points and the selection of the reference node has been analyzed by Kwok [7]. Each effect of the two factors

on the matrix (TR) was obtained by considering a global coordinate and corresponding local coordinate and the transformation between the coordinate systems. A function $f(r,z)$ defined in a region of a global r - z plane can be related to the simple local coordinates in the α - β plane as shown in Fig. 7. The nine points in the local coordinates are numbered in an arbitrary order. The coordinate (α_i, β_i) in the local plane corresponds to the coordinate (r_i, z_i) in the global plane. Within the local curvilinear mesh, the function value for an arbitrary point can be approximated with the following second-order polynomial:

$$f = a_1 + a_2\alpha + a_3\beta + a_4\alpha^2 + a_5\beta^2 + a_7\alpha^2\beta + a_8\alpha\beta^2 + a_9\alpha^2\beta^2. \quad (4.2.5)$$

From the equations for the nine nodal points, the coefficients in Eq. (4.2.5) are known and then the first and second derivatives with respect to α and β are given in terms of the coefficients and the function values, (f_N) . If the function in a global plane is approximated with a second-order truncated Taylor series expansion, the derivatives in the plane are expressed in terms of the global coordinates of the nine points and the function values at these points, (f_N) . The matrix (TR) was obtained by combining the derivatives in the local and global planes. The relationship between (GD) and (f_N) derived by Kwok [7] is,

$$(GD) = ((DC)(D))^{-1} (DC)(f_N) \quad (4.2.6)$$

where

$$(DC) = \begin{pmatrix} 0 & 1 & 0 & 2\alpha & 0 & \beta & 2\alpha\beta & \beta^2 & 2\alpha\beta^2 \\ 0 & 0 & 1 & 0 & 2\beta & \alpha & \alpha^2 & 2\alpha\beta & 2\alpha^2\beta \\ 0 & 0 & 0 & 2 & 0 & 0 & 2\beta & 0 & 2\beta^2 \\ 0 & 0 & 0 & 0 & 0 & 1 & 2\alpha & 2\beta & 4\alpha\beta \\ 0 & 0 & 0 & 0 & 2 & 0 & 0 & 2\alpha & 2\alpha^2 \end{pmatrix} A^{-1} \quad (4.2.7)$$

$$(D) = \begin{pmatrix} h_1 & k_1 & h_1^2/2 & h_1k_1 & k_1^2/2 \\ h_2 & k_2 & h_2^2/2 & h_2k_2 & k_2^2/2 \\ \vdots & \vdots & \vdots & \vdots & \vdots \\ h_9 & k_9 & h_9^2/2 & h_9k_9 & k_9^2/2 \end{pmatrix} \quad (4.2.8)$$

for the central, forward as well as backward differencing schemes for various cases are obtained simply by varying m . Other parameters are dependent on m .

Fig. 8 shows nodes located at the corners and the boundaries of the computation domain as well as inside the domain. A represents the internal nodes as shown with solid circles; B , C , D and E represent the nodes along the four sides forming the boundary. There are also four corner points, F , G , H and I shown with circles. This classification is essential to employ adequate finite difference approximations to the nodes enclosed in the computational domain.

Table I. Coordinates in the α - β plane corresponding to selected reference node.

Location	Point	Node m	α	β
Internal	A	1	0	0
Boundary	B	2	1	0
	C	3	0	1
	D	4	-1	0
	E	5	0	-1
Corner	F	6	1	-1
	G	7	1	1
	H	8	-1	1
	I	9	-1	-1

Adequate difference schemes are obtained by varying only m . For an interior point, a central difference formula is employed; but, for the nodes located along the boundaries

and at the corners, a forward or backward differencing technique is used to retain the second-order accuracy of the derivative approximations. The proper selection of m for different cases and corresponding α and β values dependent on m are listed in Table I.

4.3 Iterative computation.

Physical properties such as viscosity, permeability, the density of the solid, and the density of interdendritic liquid are temperature dependent. The composition of the interdendritic liquid is also related to temperature by the liquidus of the phase diagram. With temperature and volume fraction liquid in the computational domain specified, the coefficients and the r.h.s. of the pressure equation (Eq. (3.4.2)) can be estimated. Then the pressures in the domain are obtained, and the velocities, which depend upon the pressure distribution, are computed using D'Arcy's Law. The volume fraction of liquid is updated to satisfy the local solute redistribution equation, and then the temperature is reestimated.

The iteration steps are performed as follows:

1. Start with a linear temperature profile in the z -direction and zero velocity. Solve for g_L .
2. Solve the pressure equation.
3. Check whether the pressure is sufficiently accurate. If the solution is accurate enough, jump to step 7.
4. Employ D'Arcy's Law to calculate velocity.
5. Recalculate g_L using the local solute redistribution equation.
6. Solve energy equation for temperature and then go back to step 2.
7. Terminate the loop.

A detailed description of these steps is given in later subsections.

4.4 Evaluation of Coefficients in Pressure Equation.

The values of α_r , α_z , β_r and β_z defined by Eq. (3.3.8) vary by several orders of magnitude in the computation domain. The derivatives of these functions are expressed in terms of their logarithms:

$$\frac{\partial \alpha_r}{\partial r} = \alpha_r \frac{\partial \ln \alpha_r}{\partial r} \quad (4.4.1)$$

$$\frac{\partial \alpha_z}{\partial z} = \alpha_z \frac{\partial \ln \alpha_z}{\partial z} \quad (4.4.2)$$

$$\frac{\partial \beta_r}{\partial r} = \beta_r \frac{\partial \ln \beta_r}{\partial r} \quad (4.4.3)$$

and

$$\frac{\partial \beta_z}{\partial z} = \beta_z \frac{\partial \ln \beta_z}{\partial z} \quad (4.4.4)$$

Finite difference approximations were applied to the logarithms of the respective functions.

4.5 Solution of Pressure Equation.

The first and second derivatives in Eq. (3.4.3) are given by its function values at the nine nodes according to Eq. (4.2.10). The transformation matrix in Eq. (4.2.10) is generated for a node and then the derivatives, $\partial \alpha_r / \partial r$, $\partial \alpha_z / \partial z$ and $\partial \beta_z / \partial z$, are evaluated through their logarithms as explained in the previous section. The derivatives $\partial \rho_L / \partial z$ and $\partial g_L / \partial z$ are also evaluated. Now the transformation matrix is utilized to form a finite difference equation corresponding the original equation (3.4.3) for the node. The equation for node (i, j) can be written in the form:

$$\sum_{l=1}^9 a_l(i, j) \hat{P}_l(i, j) = f(i, j) \quad (4.5.1)$$

where

$$\hat{P}_l(i, j) = \hat{P}_{i+\alpha, j+\beta} \quad (4.5.2)$$

and $f(i, j)$ is the computed value of the right hand side of equation (3.4.3). The values of α and β correspond to the m as shown in Table 1. To simplify expressions, let's drop the indices i and j in Eq. (4.5.1) and rewrite

$$\sum_{l=1}^9 a_l \hat{P}_l = f. \quad (4.5.3)$$

The internal nodes are handled with Eq. (4.5.3); however, additional considerations must be given to the nodes located at boundaries. The conditions to be satisfied in developing a finite difference equation are a) the maintenance of second-order accuracy in the approximation of the pressure equation Eq. (3.4.3); b) the incorporation of the supplied boundary condition; and c) the assurance of the stability assembled matrix equation.

The derivative boundary conditions given at the eutectic isotherm, the center, and at the wall of the cylinder are of concern. The finite difference expressions for the derivatives $\partial \hat{P} / \partial r$ and $\partial \hat{P} / \partial z$ can be written

$$\frac{\partial \hat{P}}{\partial r} = \sum_{l=1}^9 s_l \hat{P}_l \quad (4.5.4)$$

and

$$\frac{\partial \hat{P}}{\partial z} = \sum_{l=1}^9 t_l \hat{P}_l \quad (4.5.5)$$

respectively, similar to Eq. (4.5.3). These equations also apply to the node (i, j) . In order to incorporate the boundary condition at $r = 0$, we solve Eq. (4.4.4) for \hat{P}_2 ,

$$\hat{P}_2 = \frac{1}{s_2} \left(\frac{\partial \hat{P}}{\partial r} - \sum_{l=1, l \neq 2}^9 s_l \hat{P}_l \right) \quad (4.5.6)$$

and when eliminate \hat{P}_2 by inserting this equation into Eq. (4.5.3). Thus,

$$\sum_{\substack{l=1 \\ l \neq 2}}^9 \left[a_l - \frac{a_2}{s_2} s_l \right] \hat{P}_l = f - \frac{a_2}{s_2} \frac{\partial \hat{P}}{\partial r} . \quad (4.5.7)$$

The derivative boundary conditions at $r = R$ and at the eutectic isotherm, as shown in Fig. 3(b), are incorporated to the finite difference Eq. (4.5.3) by following the same procedure. When several conditions are to be incorporated, e.g. for the corner points in a computational domain, the above procedure is repeated to generate a desired equation.

Finite difference approximations for all nodes are arranged to form a matrix equation. If the approximations are written in row-first order, the equation is

$$(A) (\hat{P}) = (B), \quad (4.5.8)$$

where

$$(\hat{P}) = (\hat{P}_{11}, \hat{P}_{12}, \hat{P}_{13}, \dots, \hat{P}_{21}, \hat{P}_{22}, \dots) \quad (4.5.9)$$

and

$$(B) = (B_{11}, B_{12}, B_{13}, \dots, B_{21}, B_{22}, \dots) . \quad (4.5.10)$$

For a computational domain discretized with five intervals in the r -direction and five intervals in the z -direction, the shape of matrix (A) would be represented as shown in Fig. 9.

It was not possible to determine the stability of the matrix equation (4.5.8); however, our test runs showed that (A) satisfies diagonal dominance, a sufficient condition for the stability of a matrix equation.

The Gauss-Seidel method is used to solve the matrix equation. For the five-point difference formula typically used for a rectangular computational domain, the function values at node (i,j) is updated at each iteration using the values at $(i-1,j)$, $(i+1,j)$, $(i,j-1)$ and $(i,j+1)$. In addition the generalized finite difference method uses function values at four corner nodes; their contributions are considered to be relatively insignificant.

4.6 Computation of velocities.

After solving the pressure equation, the components of velocity, V_r and V_z , are computed from Eqs. (3.3.4) and (3.3.5), respectively. However, from a numerical point-of-view, there is a difficulty in calculating an accurate value of $\partial \hat{P} / \partial z$. Fig. 10 shows a typical plot of $-\partial \hat{P} / \partial z$ and $-(\rho_L - \rho_{Lo}) g_z$ in the z -direction. The difference of the two values is quite small compared with their values. If the value of $-\partial \hat{P} / \partial z$ is slightly overestimated, e.g. five percent larger, the dotted line may lie above the solid line, leading to a velocity of opposite sign, and multiplication with a large coefficient, $K_z / (\mu g_L)$ in Eq. (3.3.5), greatly magnifies the error. In fact this happened when the derivative was estimated from the usual second order finite difference formulae. Even the sign of the velocities were reversely occasionally. This was tested against an analytical solution available for unidirectional solidification.

To overcome this problem interpolation formulas were developed. A schematic plot of \hat{P} along the z -direction, shown in Fig. 10, indicates that special consideration is mandatory due to a rapid change of \hat{P} . Data points represented with the coordinates (z_1, \hat{P}_1) , (z_2, \hat{P}_2) , ..., (z_n, \hat{P}_n) may be expressed with a polynomial

$$\hat{P} = \sum_{i=0}^{n-1} C_i z^i \quad (4.6.1)$$

where $C_0, C_1, C_2, \dots, C_{n-1}$ are the coefficients which can be readily obtained. Then the derivative is given by

$$\frac{\partial \hat{P}}{\partial z} = \sum_{i=1}^{n-1} i C_i z^{i-1} \quad (4.6.2)$$

The value of the derivative was estimated with areasonable accuracy from this equation.

4.7 Quadratic Interpolation.

A curve crossing three points (x_1, f_1) , (x_2, f_2) and (x_3, f_3) can be interpolated by a quadratic equation,

$$f = ax^2 + bx + c \quad (4.7.1)$$

with the coefficients a , b and c given by

$$a = -\frac{f_1 x_{23} + f_2 x_{31} + f_3 x_{12}}{x_{12} x_{23} x_{31}} \quad (4.7.2)$$

$$b = \frac{f_1 x_{23}(x_2 + x_3) + f_2 x_{31}(x_3 + x_1) + f_3 x_{12}(x_1 + x_2)}{x_{12} x_{23} x_{31}} \quad (4.7.3)$$

and

$$c = -\frac{f_1 x_{23} x_2 x_3 + f_2 x_{31} x_1 x_3 + f_3 x_{12} x_1 x_2}{x_{12} x_{23} x_{31}} \quad (4.7.4)$$

where

$$x_{12} = x_1 - x_2; \quad x_{23} = x_2 - x_3; \quad x_{31} = x_3 - x_1 .$$

When the relationship between x and f is given with a table of discrete points, it is necessary to employ an interpolation to obtain values of the function at a specified coordinate.

Hence, this interpolation is used to improve the estimation of a function.

4.8 Estimation of Volume Fraction Liquid.

Eq. (3.4.4) may be written

$$\frac{\partial \ln g_L}{\partial z} = q \quad (4.8.1)$$

where

$$q = \frac{\rho_L}{\rho_S (1-k)} \left[\frac{V_r}{u_z} \frac{\partial \ln C_L}{\partial r} + \left(\frac{V_z}{u_z} - 1 \right) \frac{\partial \ln C_L}{\partial z} \right] \quad (4.8.2)$$

By integrating Eq. (4.8.1) setting the lower bound of the integration to $z = z_L$, $g_L = 1$, we obtain

$$\ln g_L = \int_{z=z_L}^z q dz . \quad (4.8.3)$$

Fig. 11 shows a typical plot of the variation of the integrand along the z -direction. The solid dots correspond to the mesh points located along the line of a constant radius. The quadratic interpolation discussed in previous subsection had to be developed and employed. The solid dots are connected through a smooth curve following the interpolation using three nearest neighboring points, and then integration was performed. The area shown in Fig. 11 is used to evaluate the integral of Eq. (4.8.3) and to obtain g_L .

4.9 Temperature Calculation.

The boundary conditions applied to the solution of the energy equation (3.6.8) are shown in Fig. 3(b). The eutectic and liquidus isotherms are maintained at T_E and T_0 , respectively. At the center of the ingot the thermal gradient in the radial direction is zero due to axial symmetry. At the wall of the ingot, a proper boundary condition is not indicated. For this report, we apply a special treatment to the points along the wall.

The radial component of the interdendritic velocity, V_r , is zero at the boundary. Thus,

the energy equation becomes

$$\begin{aligned} \kappa_r \frac{\partial^2 T}{\partial r^2} + \kappa_z \frac{\partial^2 T}{\partial z^2} + \left(\frac{\kappa_r}{r} + \frac{\partial \kappa_r}{\partial r} \right) \frac{\partial T}{\partial r} + \frac{\partial \kappa_z}{\partial z} \frac{\partial T}{\partial z} \\ = -L\rho_S u_z \frac{\partial g_L}{\partial z} - \rho_L g_L (u_z - V_z) \frac{\partial L}{\partial z} - (\bar{p}u_z - \rho_L g_L V_z) \frac{\partial H_s}{\partial z} \end{aligned} \quad (4.9.1)$$

Because we are primarily interested in subtle radial gradient, we ignore radial conduction terms and keep only those in the z-direction; thus we approximate the behavior along the wall with

$$\begin{aligned} \kappa_z \frac{\partial^2 T}{\partial z^2} + \frac{\partial \kappa_z}{\partial z} \frac{\partial T}{\partial z} \\ = -L\rho_S u_z \frac{\partial g_L}{\partial z} - \rho_L g_L (u_z - V_z) \frac{\partial L}{\partial z} - (\bar{p}u_z - \rho_L g_L V_z) \frac{\partial H_s}{\partial z}. \end{aligned} \quad (4.9.2)$$

4.10 Macrosegregation Calculation.

Refer to the plot of C_S^* versus g_S in the z-direction shown in Fig. 12. Solid dots correspond to calculated results at mesh points. As g_S goes to zero, the dots are more sparsely distributed. Estimation of the local average composition after complete solidification requires the estimation of the area in Fig. 12 according to Eq. (3.7.2). Again a smooth curve connecting the dots is drawn according to the quadratic interpolation. A numerical integration for the area under the curve gives the average concentration of solute in the primary phase after solidification is complete.

4.11 Termination of iterations.

It is necessary to predict whether the current solution is sufficiently accurate. Represent the calculated \hat{P} for a point (i, j) at the n th iteration level with $\hat{P}_{i,j}^{(n)}$. The stopping

criterion employed is

$$\sqrt{\frac{\sum^{all} \left(e_{i,j}^{(n+1)} \right)^2}{\sum^{all} \left(\hat{P}_{i,j}^{(n)} \right)^2}} < \epsilon_2 \quad (4.11.1)$$

where ϵ_2 is the tolerance measured in relative error. The summation is done for all mesh points. The residual $e_{i,j}^{(n+1)}$ computed at the $(n+1)th$ iteration corresponds to $\hat{P}_{i,j}^{(n)}$. This value is used to update \hat{P} estimated at the previous iteration, i.e.

$$\hat{P}_{i,j}^{(n+1)} = \hat{P}_{i,j}^{(n)} + e_{i,j}^{(n+1)} \quad (4.11.2)$$

When Eq. (4.11.1) is satisfied, the iterations are stopped. After the first iteration, however, the next is done without checking the condition (4.11.1). A maximum number of iteration is also specified to prevent from accidental infinite looping of the iterations.

5 EMPLOYING THE CODE

The program was written primarily to investigate the effect of a very small deviation from horizontal liquidus and eutectic isotherms on the macrosegregation of Pb-Sn alloys for solidification rates ranging from 10^{-2} to 10^{-4} cm·s⁻¹. It is absolutely important to use adequate data for the density of solid, the density of interdendritic liquid, permeability, viscosity, dendrite arm spacing, thermal conductivities of solid and interdendritic liquid, phase diagram, and enthalpies of the solid and the interdendritic liquid. Data for the Pb-Sn alloys are presented in the APPENDIX. Other binary alloys can be processed by replacing thermal property data, and similar geometries of solid/liquid zone, consistent with two-dimensional (r,z) cylindrical coordinates, can be processed by modifying the grid generation procedure. The program was written in TURBO PASCAL v3.0 (Borland

International, CA) to run with a PC-DOS operating system. Graphics routines were developed using TURBO GRAPHIX V1.0 (Borland International, CA). This program can be run with IBM PC, XT, AT computers or compatibles with IBM-compatible graphics adaptor or a Hercules monochrome graphics card. A dot-matrix printer is necessary to get hardcopies of plots displayed on screen. For higher speed computations, installation of the 8087 (80287 for AT machines) math coprocessor is recommended.

5.1 Program Options (Menus).

When execution of this program is requested, a menu is displayed on the screen and instructs the operator to make a selection. This menu is reproduced as Fig. 13. A brief description of each option is given below.

0: Concise description of the program is displayed on screen. This can be sent to printer by pressing Shift-PrtSc key.

1: Requests the operator to enter the name of the input and output data filenames.

Currently PB-SN.DAT is the only file which can be accessed. After execution of this option, the name of the files and the message "NO results yet" are displayed on the screen (Fig. 14).

2: The data read from the parameter file is displayed on the screen (Fig. 15). The operator can modify any of these parameters or get a hardcopy of the data. The definitions of the parameters are given below:

C_0 : weight percent Sn.

R, a, b, z_{L0} : geometry of the solid/liquid zone (Fig. 5).

u_z : solidification rate, $\text{cm} \cdot \text{s}^{-1}$.

hzref : ratio of the adjacent grid spacings in the z-direction. The grid spacings can be gradually reduced by setting it to a value less than unity. Recommended value ranges from 0.8 to 1.0.

tol : tolerance allowed given in terms of relative error.

maxitr : maximum number of iterations.

kmodel : permeability model. Several permeability models will be implemented in future versions; however, there is currently only one option available.

mmax : number of subintervals in the r-direction for the mesh.

nmax : number of subintervals in the z-direction for the mesh.

ENERGY : Energy equation may be solved (**ENERGY=1**) or the temperature variation along the z-direction is assumed to be linear (**ENERGY=0**).

DEBUG : Intermediate results are displayed on the screen or printer if this variable is not zero. This feature was used to facilitate program debugging.

DEVICE : Intermediate results can be displayed on the screen (**DEVICE=0**) or sent to the printer (**DEVICE=1**). This feature is also used for program debugging.

3: Now, we return to Fig. 13. The data updated by selecting option 2 is overwritten to the parameter file.

4: The operator can switch to other input and output parameter files for the program run. This option would be useful when the program is extended to process

various binary alloys.

- 5: Program is run and intermediate and final results are stored as disk files.
- 6: Final results are displayed on the screen. Also hardcopies of these results may be obtained.
- 7: Exit to the operating system (DOS).

5.2 Output.

The results obtained with the parameters displayed on Fig. 15 are shown in Fig. 16. The effects of solidification process parameters on macrosegregation are under analysis. Here the intent is to merely acquaint the reader with the mechanics of using the program.

Fig. 16(a) shows the mesh and the velocity vectors of the interdendritic liquid. The center of the ingot ($r=0$) is to the left, and the wall ($r=R$) is to the right. Notice that the isotherms, Fig. 16(b), are slightly convex so the less dense interdendritic liquid, enriched in Sn, flows toward the center. Fig. 16(c) gives the temperature along the center-line and along the surface. For this example, it is almost linear, but at greater solidification velocities the deviation from linearity is more noticeable. The outputs likely to be of most interest to the users of this program, are shown in Figs. 16(d) and (e) for the concentration of Sn and volume fraction of eutectic, respectively. Consistent with the flow of the interdendritic liquid, Fig. 16(a), the amount of eutectic and the composition increase from the wall to the center. Finally, other characteristics of the mushy zone are given by Figs. 16(f) through 16(h).

REFERENCES

1. M. C. Flemings and G. E. Nereo: Trans. TMS-AIME, 1967, vol. 239, pp. 1449-61.
2. A. L. Maples and D. R. Poirier: Metall. Trans., ,1984, vol. 5B, pp. 163-172.
3. M. K. Hubbert: Petroleum Trans., AIME, 1956, vol. 236, pp. 222-239.
4. D. R. Poirier: Metall. Trans. B, 1987, vol. 18B, pp. 245-255.
5. S. Kou: Ph.D. Thesis, Massachusetts Institute of Technology, 1978.
6. S. D. Ridder, S. Kou and R. Mehrabian: Metall. Trans. B, 1981, vol. 12B, pp. 435-447.
7. S. K. Kwok: Computational Techniques and Applications, CTAC-83, Ed. by J. Noye & C. Fletcher, Elsevier Science Publishing, North-Holland, 1984, pp. 173-181.
8. D. R. Poirier: submitted for publication.
9. H. J. Fecht and J. H. Perepezko: Metall. Trans. A, vol. 19A, to be published.
10. H. R. Thresh, A. F. Crawley and D. W. G. White: Trans. Met. Soc. AIME, 1968, vol. 242, pp. 819-822.
11. W. D. Drotning: High Temp. Sci., 1979, vol. 11, pp. 265-276.
12. A. E. Schwaneke, W. L. Falke and V. R. Miller: J. Chem. Eng. Data, 1978, vol. 23, pp. 298-301.
13. H. R. Thresh and A. F. Crawley: Metall. Trans. 1970, vol. 1, pp. 1531-35.
14. Metals Handbook, 8th edition, vol. 1, Americal Society for Metals, Metals Park, Ohio, 1961, pp. 1064 and 1144.
15. J. T. Mason, J. D. Verhoeven and R. Trivedi: J. of Crystal Growth, 1982, vol. 59, pp. 516-524.

16. E. A. Brandes (ed.): *Smithells Metals Reference Book*, 6th ed., Butterworths, London, 1983, pp. 14-1 to 14-2.
17. D. R. Poirier and P. Nandapurkar: submitted for publication.

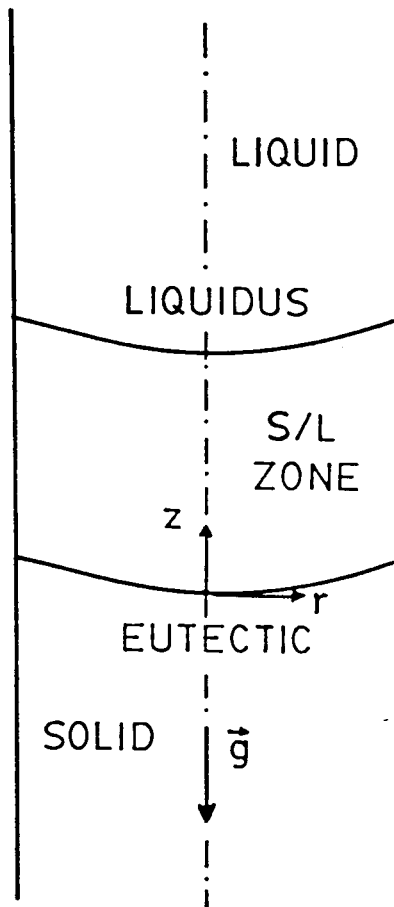


Fig. 1 Vertical solidification of melt in cylindrical mold.

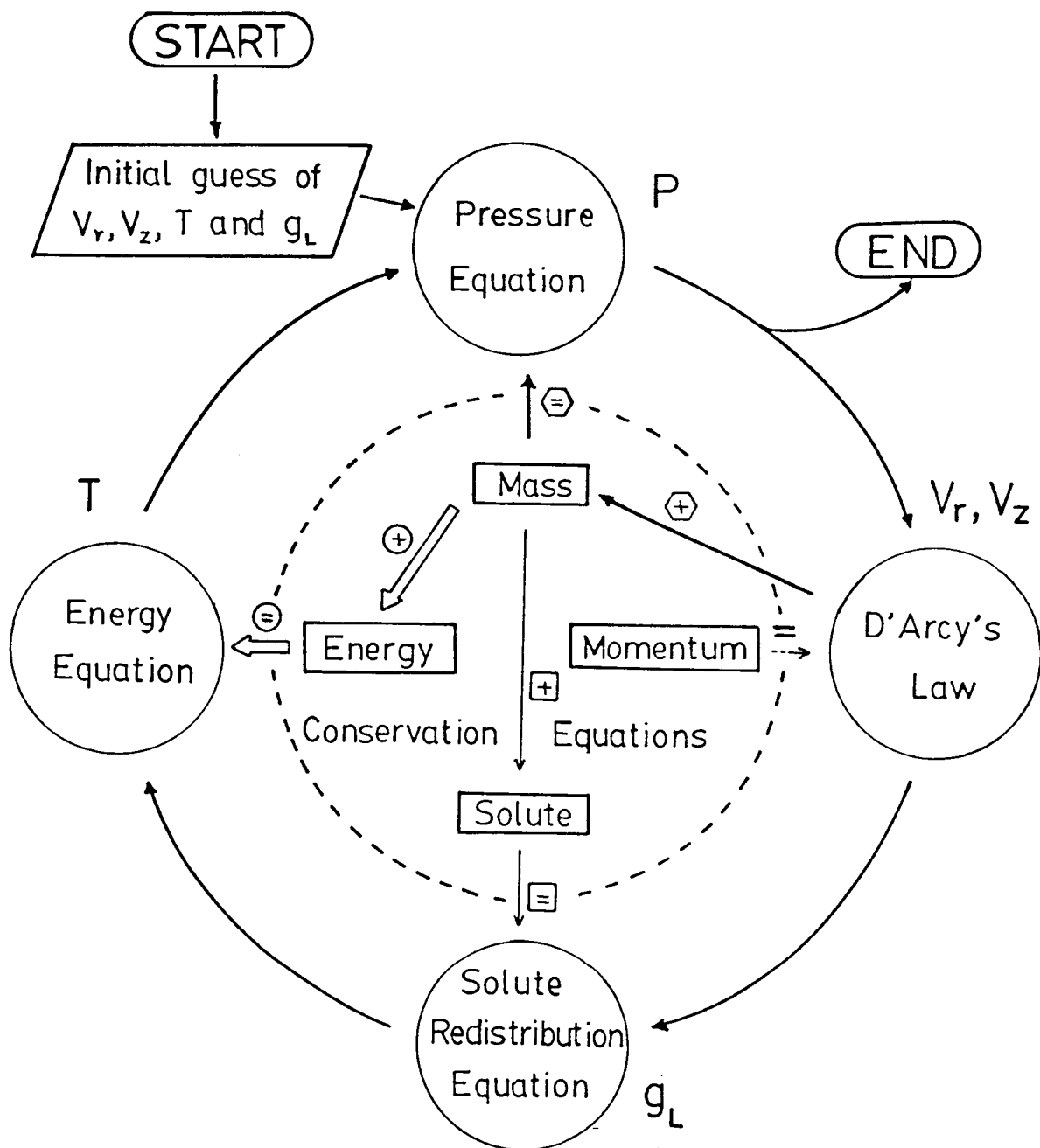


Fig. 2 Formulation of flow equations.

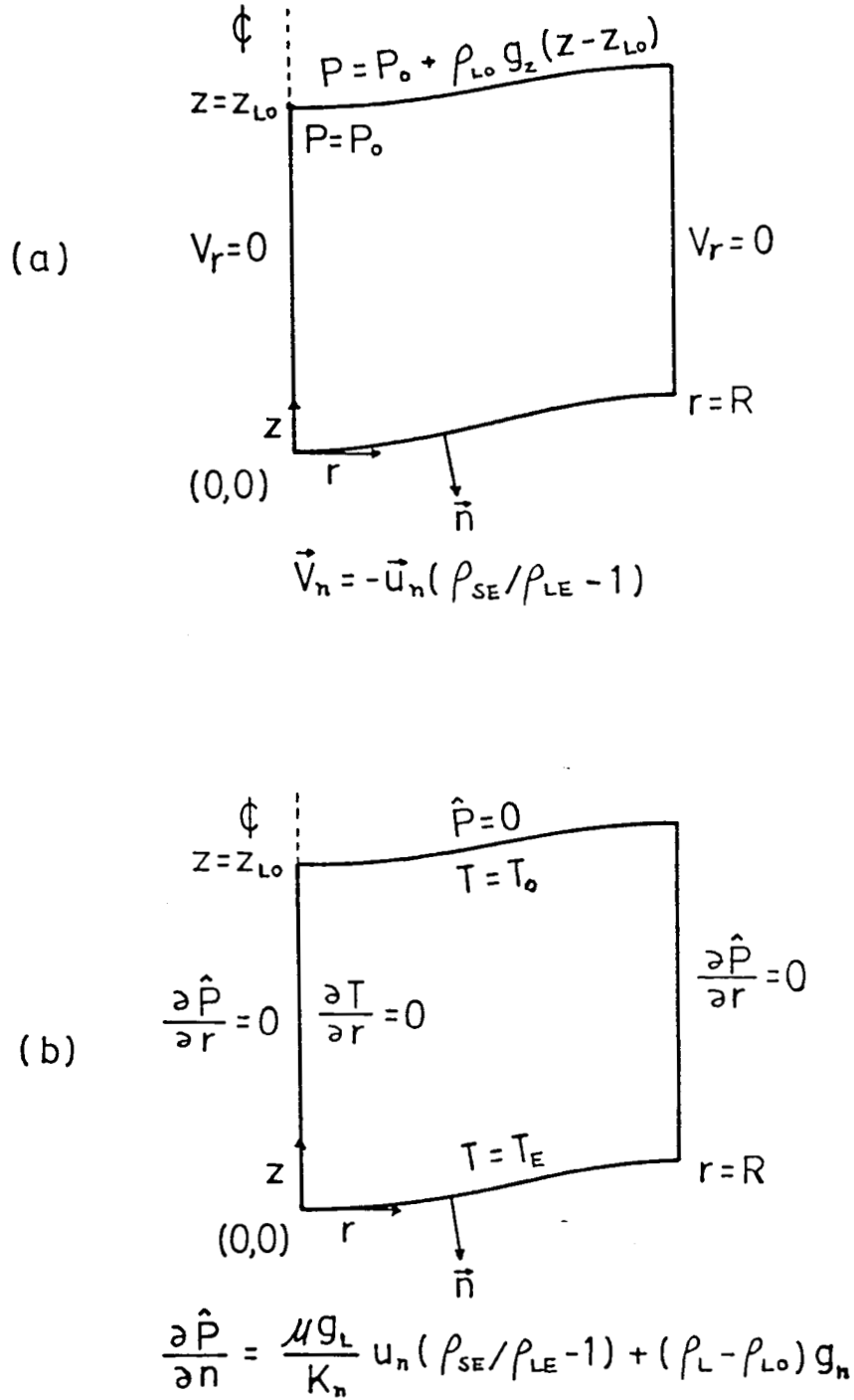


Fig. 3 Boundary conditions given in (a) original and (b) transformed coordinate systems.

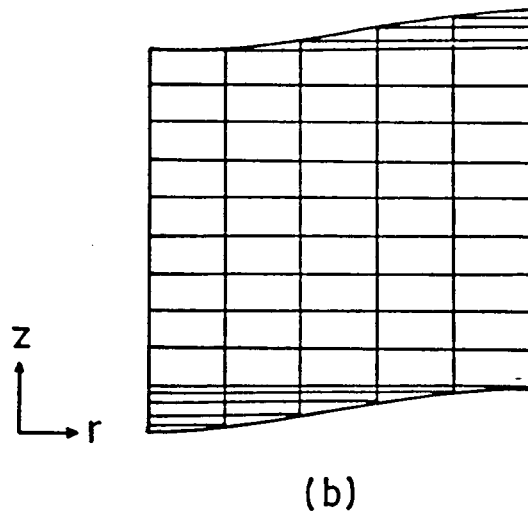
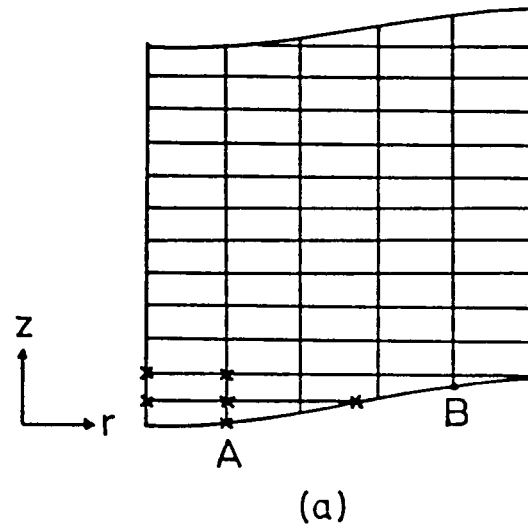


Fig. 4 Rectangular meshes
 (a) uniform spacings in both directions
 (b) uniform spacings in the r -direction,
 but adjusted nonuniform spacings in the
 z -direction.

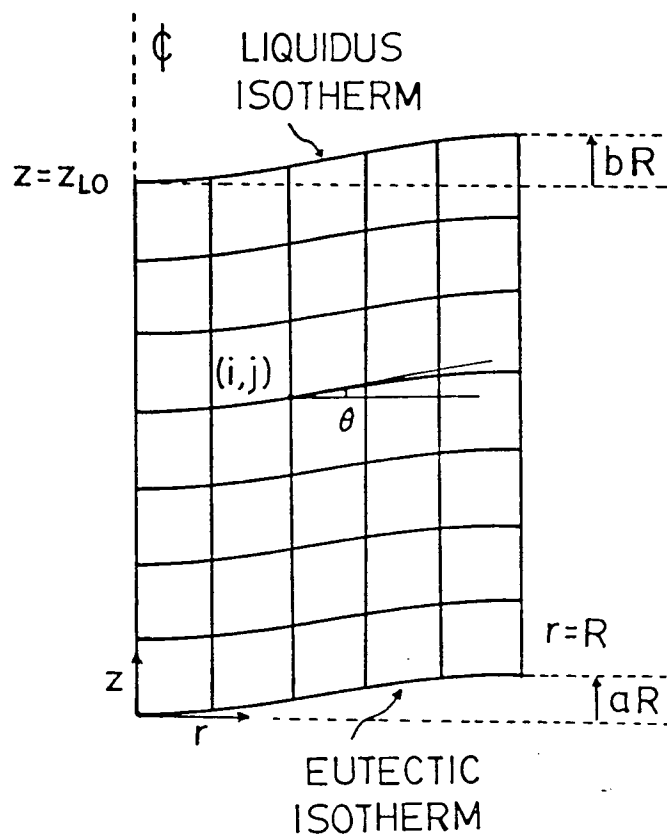


Fig. 5 Computational mesh.

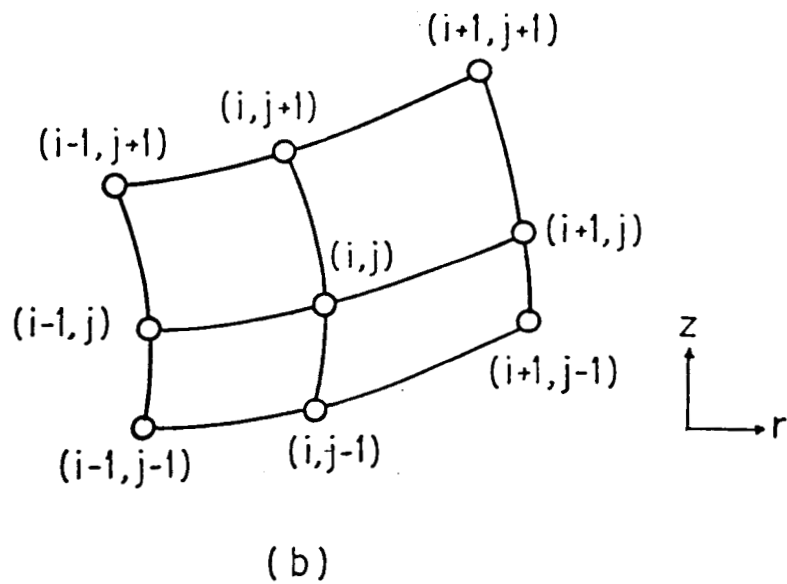
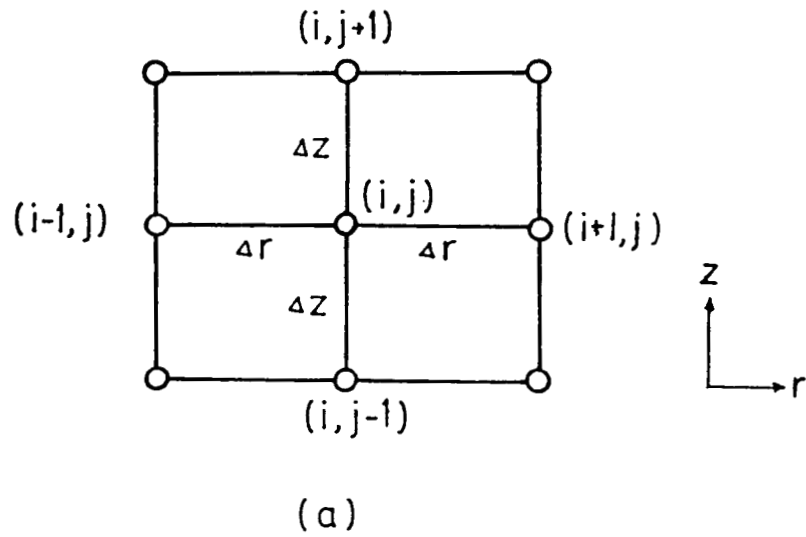


Fig. 6 Finite difference formulations for
 (a) an orthogonal rectangular mesh, and
 (b) a nonorthogonal irregular mesh.

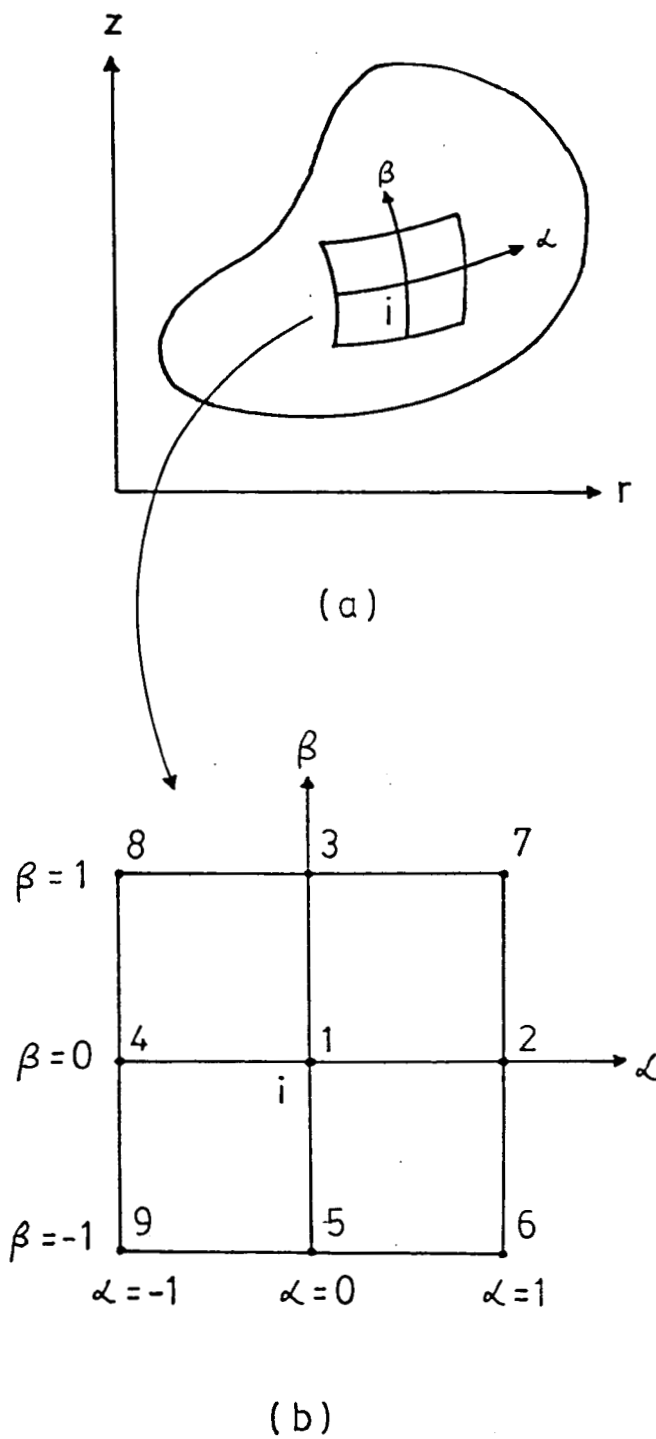


Fig. 7 Curvilinear nine-point mesh in
 (a) global r - z plane, and
 (b) local ξ - β plane at node i .

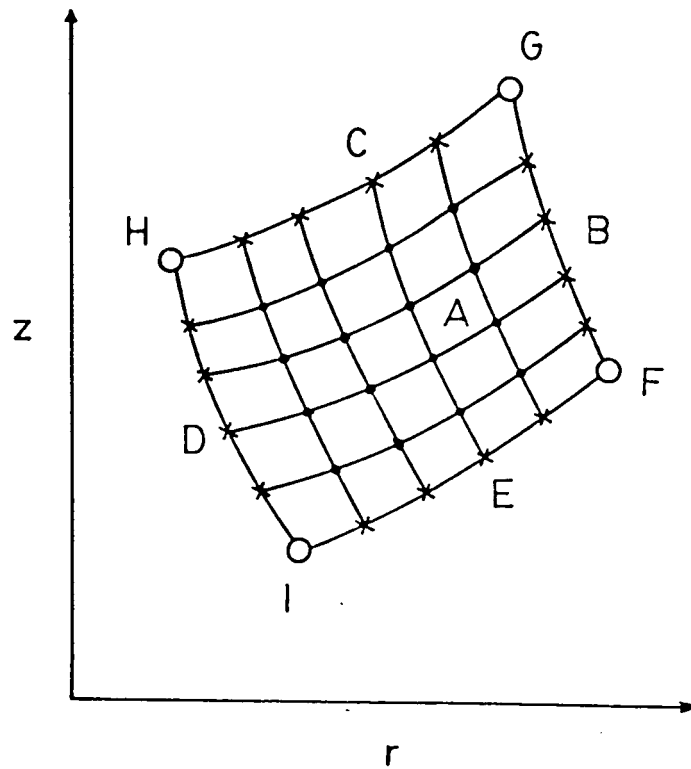


Fig. 8 Classification of mesh points in computation domain;

. : internal
 o : corner
 x : side

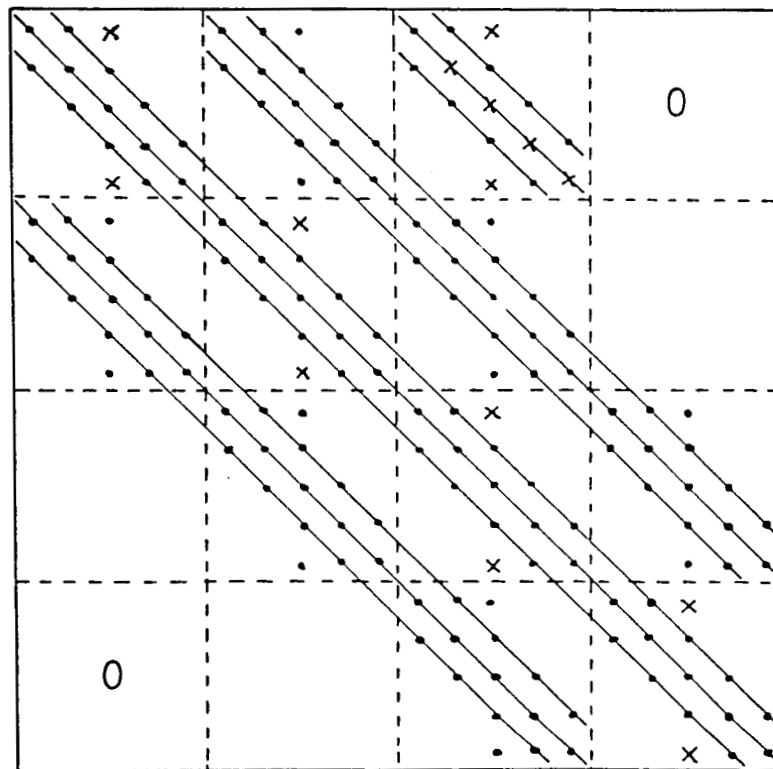


Fig. 9 The shape of matrix A .
 . : nonzero elements.
 x : elements reduced to zero by incorporating
 derivative boundary conditions.

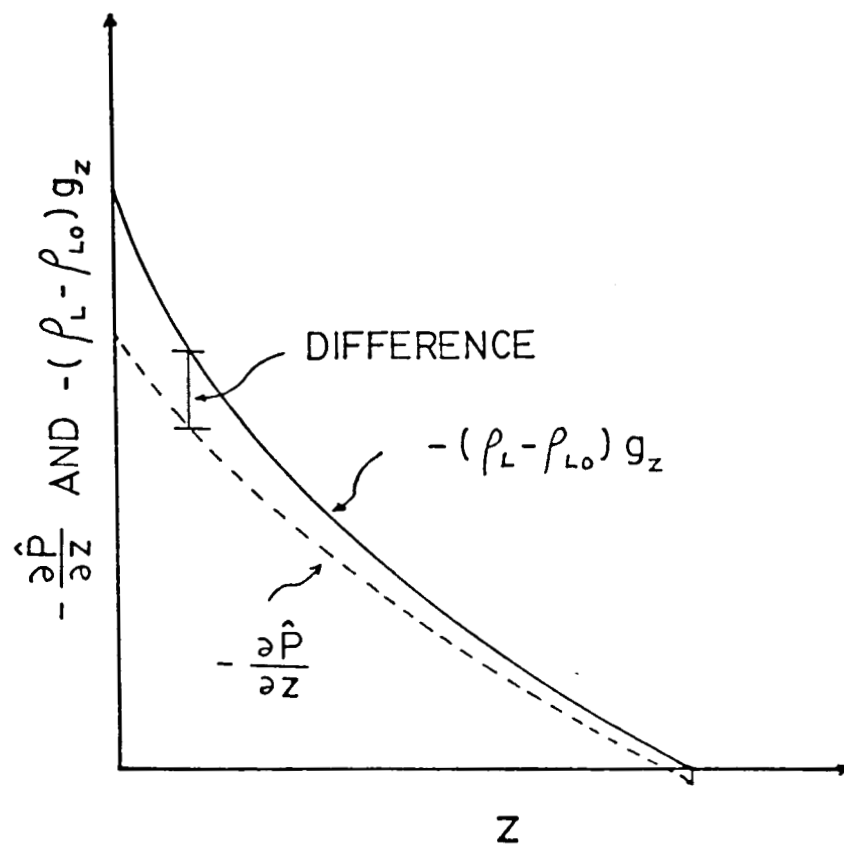


Fig. 10 Comparison of $-\frac{\partial \hat{P}}{\partial z}$ and $-(\rho_L - \rho_{L0}) g_z$

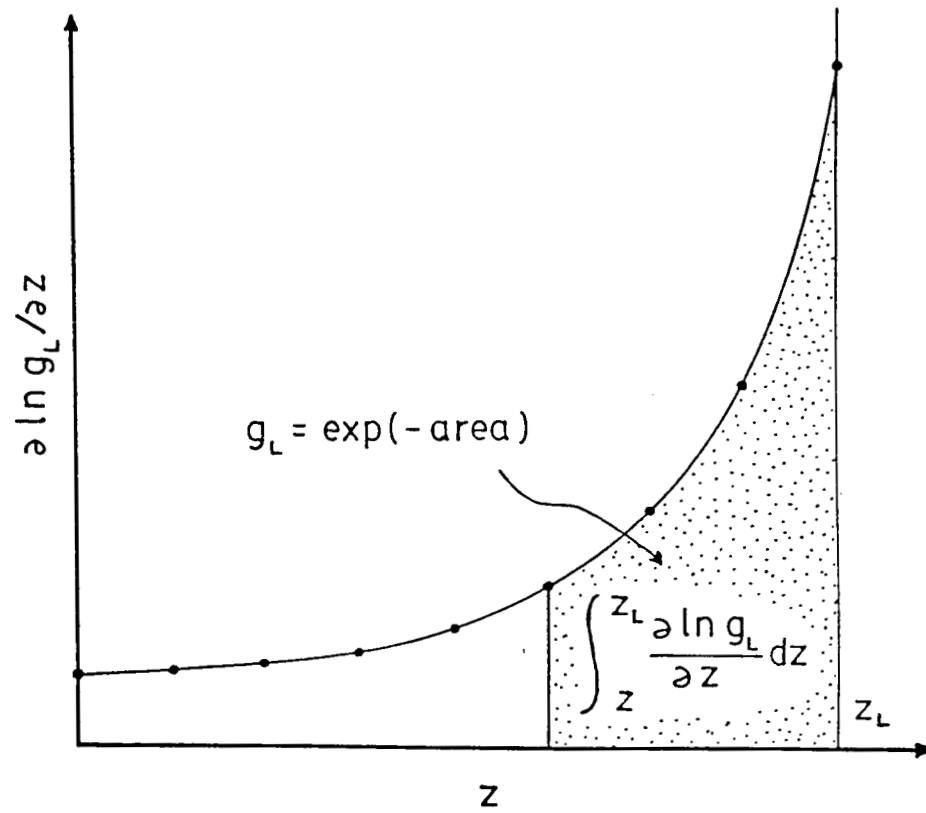


Fig. 11 Estimation of volume fraction liquid by integration. Solid dots correspond to mesh points.

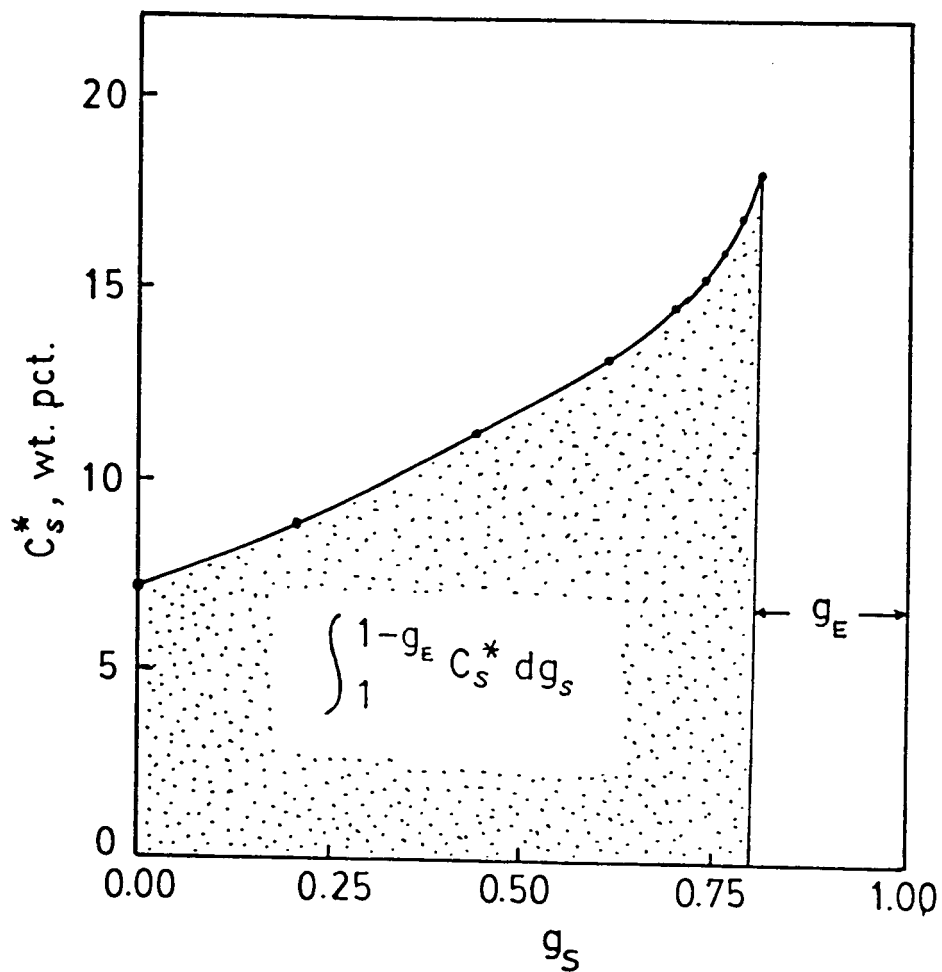


Fig. 12 Plot of C_s^* versus g_s in the z-direction.
Solid dots correspond to mesh points.

----- MENU -----

- 0. Display background information
- 1. Read input parameters
- 2. Modify input parameters
- 3. Save updated parameters
- 4. Goto other parameter file
- 5. Run program
- 6. Plot final results
- 7. Quit

NO parameter data exists.

INPUT FILENAME :
OUTPUT FILENAME :

Enter your selection :

Fig. 13 Menu displayed on screen at the beginning of program run.

----- MENU -----

- 0. Display background information
- 1. Read input parameters
- 2. Modify input parameters
- 3. Save updated parameters
- 4. Goto other parameter file
- 5. Run program
- 6. Plot final results
- 7. Quit

NO results yet.

INPUT FILENAME : pb-sn.dat
OUTPUT FILENAME : m09

Enter your selection :

Fig. 14 Menu displayed on screen after selection of menu "1", and input and output filenames.


```

PARAMETER DATA
-----
1.      C0      15.0000
2.      R       1.0000
3.      a      -0.3000
4.      b      -0.3000
5.      zL       5.0000
6.      Uz     4.00E-004
7.      hzref   1.00E+000
8.      tol     1.00E-006
9.      maxitr      10
10.     kmodel      1
11.      mmax       8
12.      nmax       8
13.     ENERGY      1
14.     DEBUG        1
15.     DEVICE       0

```

Which one? (1 to 15) :

PARAMETER FILE : pb-sn.dat

Changed 2 times.

Enter 0 to stop changing.

Enter > 15 to print screen.

Fig. 15 Display of the data read from parameter file when menu "2" is selected. Operator can change the input parameters.

ORIGINAL PAGE IS
OF POOR QUALITY

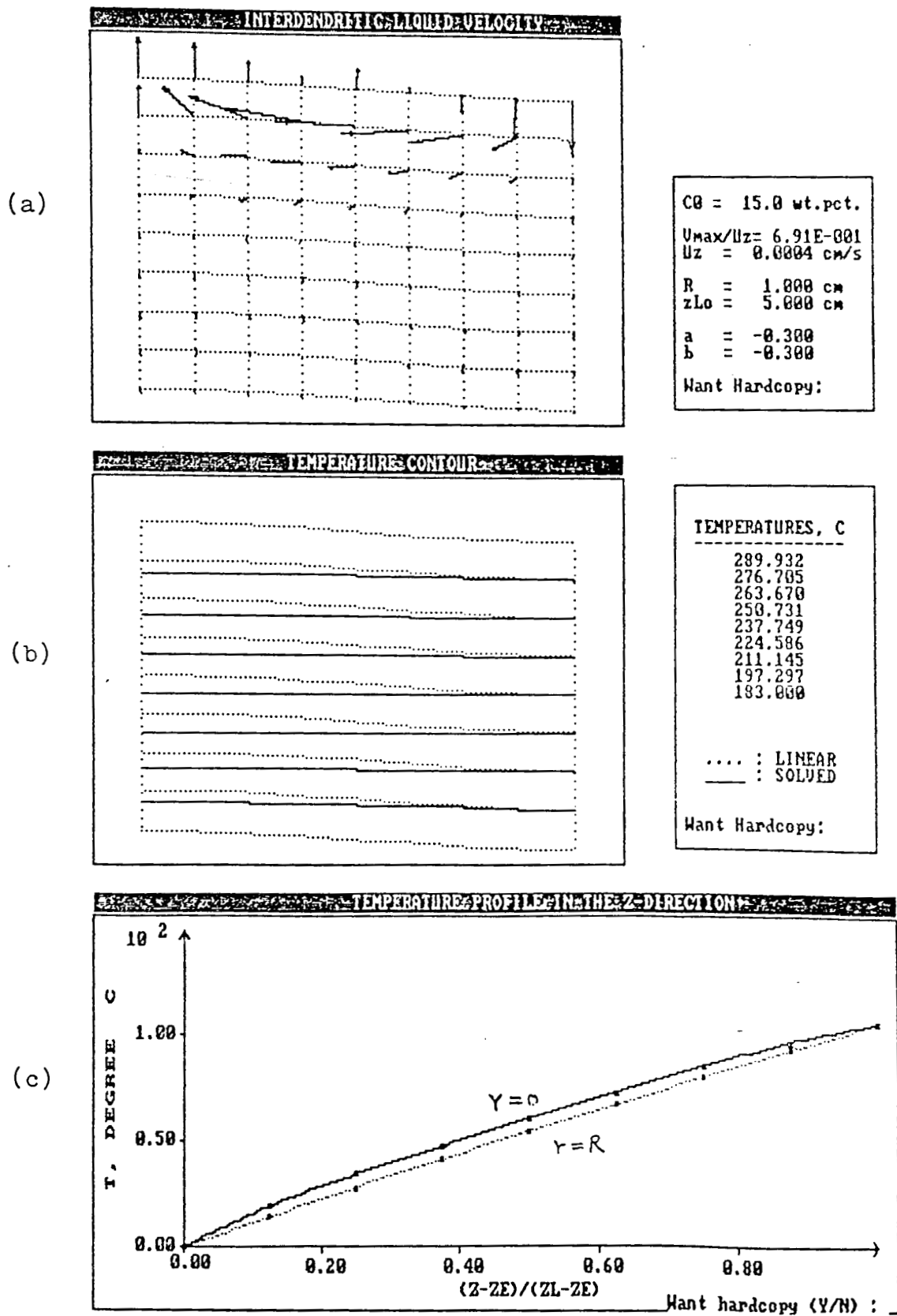


Fig. 16 Output obtained from the parameters shown in Fig. 14.

ORIGINAL PAGE IS
OF POOR QUALITY

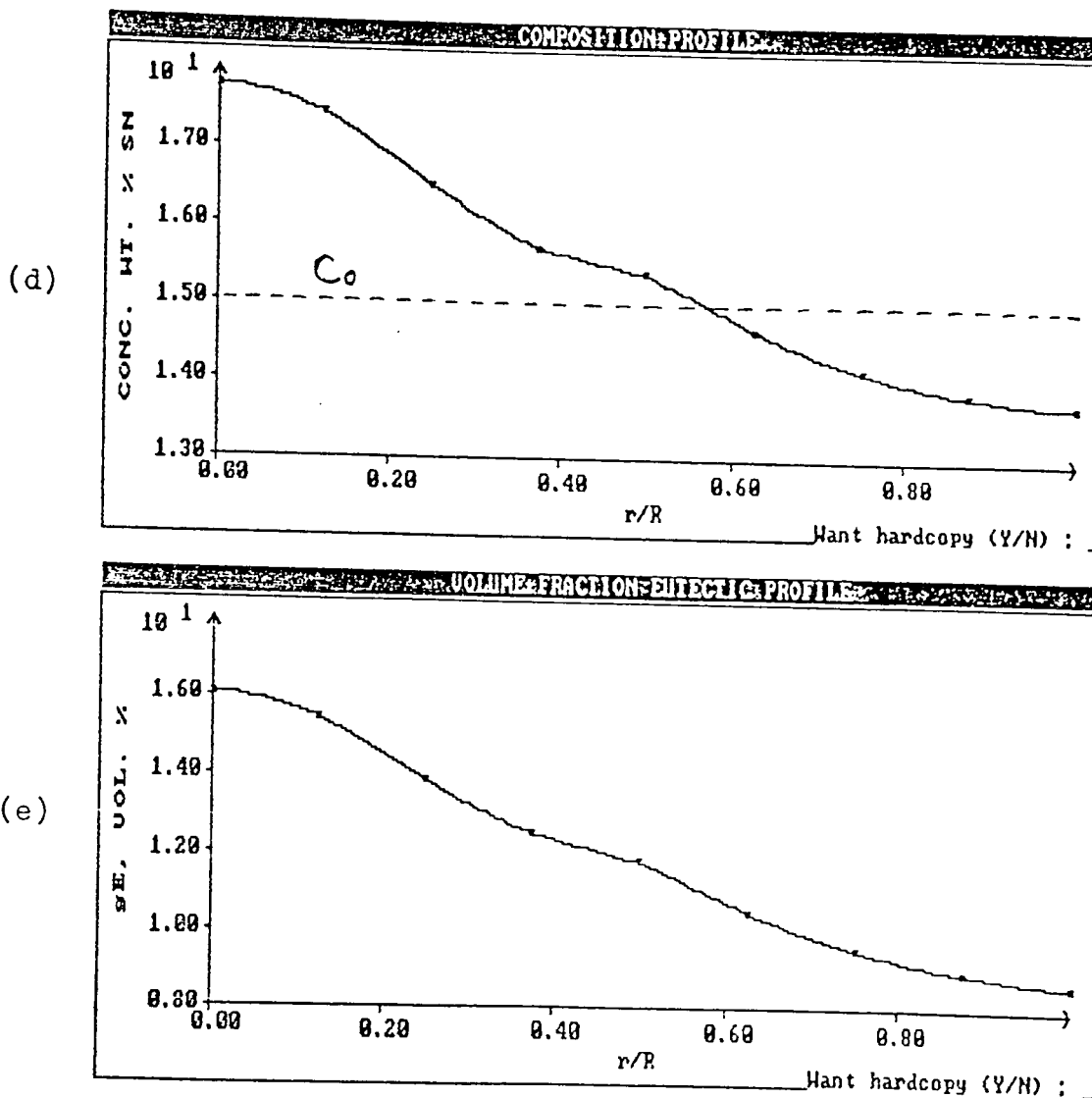
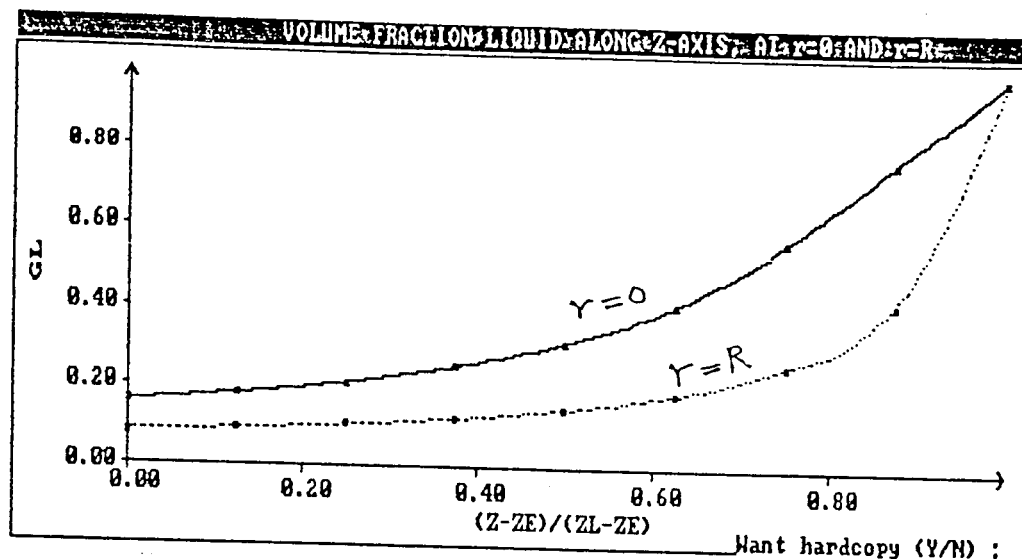


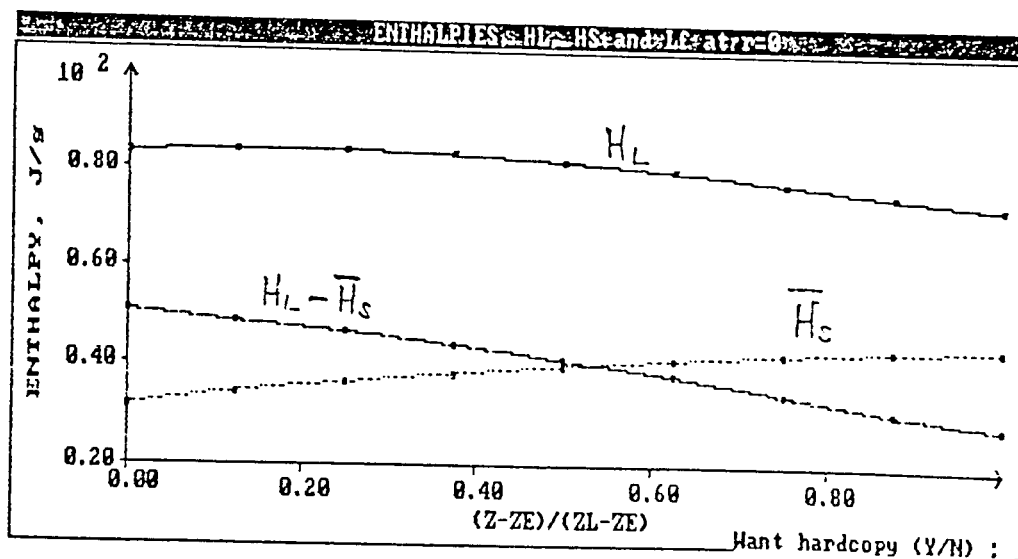
Fig. 16 (continued.)

ORIGINAL PAGE IS
OF POOR QUALITY

(f)



(g)



(h)

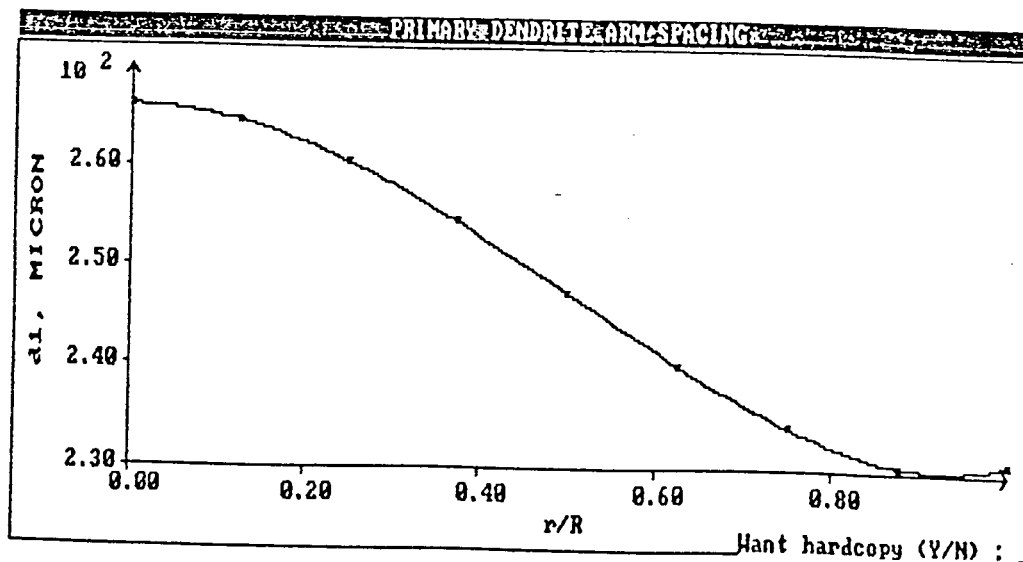


Fig. 16 (continued.)

APPENDIX - DATA FOR PB-SN ALLOY

A.1 Density of Solid.

$$\rho_{SE} \text{ (density of eutectic solid)} = 8.366 \text{ g/cm}^3$$

$$\rho_S \text{ (average density of solid)} = 11.340 - 0.05898 \overline{C}_s - 0.001273 T$$

The density of the solid (lead-rich α phase) is determined by Poirier [8] using lattice parameters reported by Fecht and Perepezko [9].

A.2 Density of Liquid.

$$\rho_{LE} \text{ (density of eutectic liquid)} = 7.928 \text{ g/cm}^3$$

$$\rho_L = 10.559 - 0.04251 C_L$$

The density of interdendritic liquid is presented as a function of C_L by Poirier [8] based upon reported [10,11,12].

A.3 Viscosity.

$$\mu = 0.026 \text{ poise } (g \cdot s^{-1} \cdot cm^{-1})$$

Thresh and Crawley [13] measured the viscosities of Pb-Sn melts and extrapolated their results to the liquidus temperatures. They found that these viscosities are almost constant; thus an average value is used here.

A.4 Phase Diagram.

Sufficient number of points were taken from the liquidus and solidus curves of the Pb-Sn equilibrium phase diagram [14] (Fig. A1) and fitted to polynomials. C_L and k are

given by,

$$C_L = 61.656 - 41.496 x - 54.929 x^2 + 34.872 x^3$$

and

$$k = 0.301 + 0.200 x - 0.443 x^2 + 0.73 x^3$$

where

$$x \equiv (T - T_E)/(T_M - T_E)$$

$$T_E = 183 \text{ } ^\circ\text{C}$$

$$T_M = 327.5 \text{ } ^\circ\text{C}$$

and

$$C_E = 61.9 \text{ wt. pct. Sn.}$$

A.5 Primary Dendrite Arm Spacing.

$$d_1 = 584 G_L^{-0.303}$$

where d_1 is in μm , and G_L in $^\circ\text{C} \cdot \text{cm}^{-1}$. Mason et al. [15] showed that primary dendrite arm spacings of dendrites in Pb-Sn alloys of various compositions. At low solidification rates of our interest, the dependency of d_1 on the solidification rate is small. Their results also indicate a weak dependency of d_1 on alloy composition. The empirical formula is for Pb-40 Sn alloy and a solidification rate of $10^{-3} \text{ cm} \cdot \text{s}^{-1}$; however, the actual dendrite arm spacing is expected to be accurate within 10 % .

A.6 Permeability of interdendritic liquid.

$$K = 3.75 \times 10^{-4} g_L^2 d_1^2$$

Poirier [4] modelled the flow of the interdendritic liquid with Hagen-Poiseuille law and estimated the relationship based on available data.

A.7 Thermal Conductivity.

The thermal conductivities of pure Pb and of Sn in the liquid and solid states, as functions of temperature, are taken from Brandes [16] and extrapolated to the temperature range, 183 °C – 327.5 °C as necessary. (See Fig. A2).

$$\kappa_s(Pb) = 0.318 - 1.85 \times 10^{-4} (T - T_E)$$

$$\kappa_l(Pb) = 0.130 + 1.64 \times 10^{-4} (T - T_E)$$

$$\kappa_s(Sn) = 0.605 - 2.99 \times 10^{-4} (T - T_E)$$

$$\kappa_l(Sn) = 0.290 + 2.01 \times 10^{-4} (T - T_E)$$

The units of these conductivities are in $watt \cdot cm^{-1} \cdot ^\circ C^{-1}$.

A.8 Enthalpy.

$$\begin{aligned} \overline{H_S} = & -4.788 + 0.13868 T + 0.97811 \overline{C_S} \\ & - 1.0332 \times 10^{-3} \overline{C_S}^2 + 1.0449 \times 10^{-3} \overline{C_S} T \quad \text{Joule/g} \end{aligned}$$

$$\begin{aligned} H_L = & 63.772 + 0.72996 C_L - 7.1156 \times 10^{-3} C_L^2 \\ & + 3.7147 \times 10^{-5} C_L^3 - 4.7423 \times 10^{-7} C_L^4 \quad \text{Joule/g} \end{aligned}$$

Poirier and Nandapurkar [17] evaluated the enthalpies of the dendritic solid and interdendritic liquid of Pb-Sn alloys and found that they are appreciably dependent on alloy composition. These dependencies were expressed in polynomials reproduced here.

ORIGINAL PAGE IS
OF POOR QUALITY

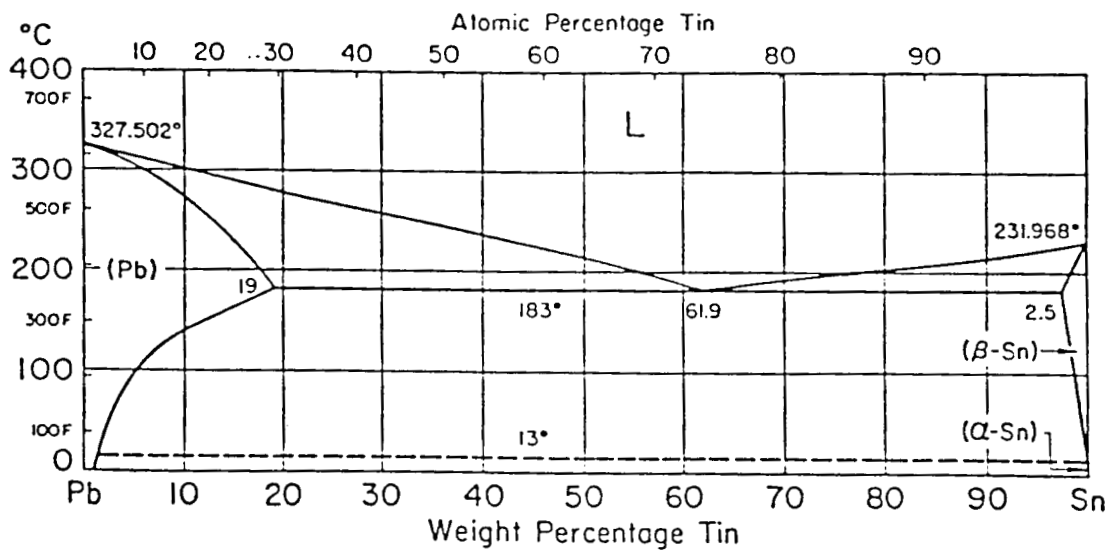


Fig. A1 The Pb-Sn equilibrium phase diagram [14].

ORIGINAL PAGE IS
OF POOR QUALITY

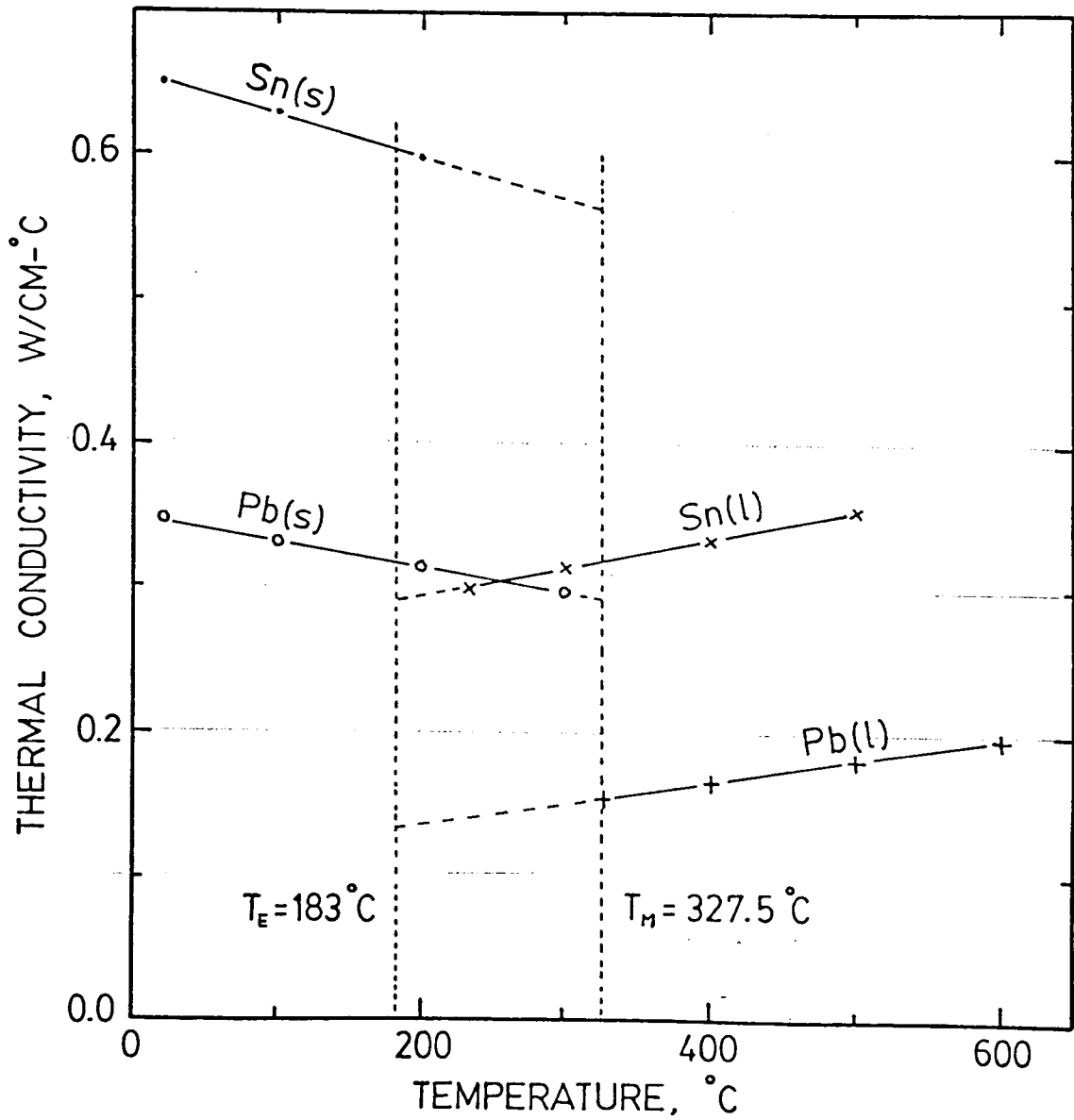


Fig. A2 Thermal conductivities of Pb and Sn in the solid and liquid states [16].